Materials Today Bio 36 (2026) 102643

Contents lists available at ScienceDirect

Materials Today Bio

journal homepage: www.journals.elsevier.com/materials-today-bio

Bioconvergence of sound-guided and supramolecular assembly strategies to create peptide-protein composite hydrogels with predictable shape-to-function features

Cosimo Ligorio [a,b,c,d], Alessandro Cianciosi [e], Riccardo Tognato [e], Micaela Natta [e], Romedi Parolini [e], Sena Ardicli [f,g], Huseyn Babayev [f], Ieva Sapjanskaite [b], Samantha L. Kilgour [h], Richard Homer [i], Bapan Pramanik [b], Zhiyu Zhou [j,k], Andrea Malandrino [l], Eleni Priglinger [l], Cezmi Akdis [f], Martin J. Stoddart [e], Alvaro Mata [a,b,c,d,*], Tiziano Serra [e,m,**]

[a] *Biodiscovery Institute, University of Nottingham, Nottingham, UK*
[b] *School of Pharmacy, University of Nottingham, Nottingham, UK*
[c] *Department of Chemical and Environmental Engineering, University of Nottingham, Nottingham, UK*
[d] *NIHR Nottingham Biomedical Research Centre, Nottingham, NG7 2UH, UK*
[e] *AO Research Institute Davos, Switzerland*
[f] *Swiss Institute of Allergy and Asthma Research (SIAF), University of Zurich, Davos, Switzerland*
[g] *Department of Genetics, Faculty of Veterinary Medicine, Bursa Uludag University, Bursa, Turkey*
[h] *School of Chemistry, University of Nottingham, Nottingham, UK*
[i] *Wolfson Building, University of Nottingham, Nottingham, UK*
[j] *Innovation Platform of Regeneration and Repair of Spinal Cord and Nerve Injury, Department of Orthopaedic Surgery, The Seventh Affiliated Hospital, Sun Yat-sen University, Shenzhen, China*
[k] *Guangdong Provincial Key Laboratory of Orthopaedics and Traumatology, Orthopaedic Research Institute/Department of Spinal Surgery, The First Affiliated Hospital of Sun Yat-sen University, Guangzhou, China*
[l] *Johannes Kepler University Linz, Kepler University Hospital, Department for Orthopaedics and Traumatology, Linz, Austria*
[m] *Complex Tissue Regeneration Department, MERLN Institute for Technology-Inspired Regenerative Medicine, Maastricht University, Maastricht, Netherlands*

A R T I C L E I N F O

Keywords:
Biofabrication
Sound-based bioassembly
Bottom-up
Peptide amphiphiles
Proteins
Composite
Multiscale

A B S T R A C T

Purely protein-based hydrogels are widely used in tissue engineering for their biomimicry and biocompatibility, yet remain challenging to tailor with precision and predictability at biological and mechanical levels. To overcome this, synthetic self-assembling peptide amphiphiles (PAs) offer opportunities for supramolecular customization, both as single-phase materials and co-assembled with proteins to create hybrid nanocomposites with emerging functionalities. Similarly, contactless, sound-guided bioassembly techniques using liquid-phase hydrogel precursors are emerging as strategic tools for obtaining structured and functional hydrogels. Leveraging these advances, here a fast, contactless, 'one-pot' bioassembly strategy merging supramolecular PA self-assembly with sound-guided patterning to fabricate hybrid peptide-protein hydrogels with predictable, shape-dependent functionality is presented. Using fibrin as proof-of-concept, material performance is biologically enhanced by incorporating growth factor-binding PAs, while inorganic microparticles are embedded and spatially organized *via* acoustic fields to tune mechanical properties. This strategy allows predictable tuning of composite stiffness and architecture by adjusting sound wave frequency, with acoustic fields guiding material organization from nano-to-macroscale. Composite hydrogels result highly permissive to cell infiltration *in vitro* and versatile platforms to tune immune cell-material interactions. This modular biofabrication platform integrating supramolecular and sound-guided processes can be generalized to other building blocks, opening unique opportunities for scalable, tunable, and hierarchically-organized biomaterials.

This article is part of a special issue entitled: Multiscale Composites published in Materials Today Bio.

* Corresponding author. Biodiscovery Institute, School of Pharmacy and Department of Chemical and Environmental Engineering, University of Nottingham, Nottingham, UK.
** Corresponding author. AO Research Institute Davos, Switzerland.
E-mail addresses: a.mata@nottingham.ac.uk (A. Mata), tiziano.serra@aofoundation.org (T. Serra).

https://doi.org/10.1016/j.mtbio.2025.102643
Received 13 October 2025; Received in revised form 1 December 2025; Accepted 6 December 2025
Available online 9 December 2025
2590-0064/© 2025 The Authors. Published by Elsevier Ltd. This is an open access article under the CC BY license (http://creativecommons.org/licenses/by/4.0/).

1. Introduction

Purely protein-based biomaterials, such as collagen and fibrin hydrogels, have historically represented a preferred choice for cell culture and tissue engineering, due to their excellent biomimicry and biocompatibility properties. Despite their widespread use, the natural origin of pure proteins makes them a challenging material to be customized with precision at both chemical and mechanical levels. For instance, proteins are known to present multiple bioactive sites, either in full-display or buried in cryptic sites, but the presentation of some epitopes over others remains a challenge due to the inherent structural complexity of proteins [1]. Similarly, the use of proteins to rationally-design materials with predictable properties remains difficult due to batch variability, hierarchical assembly, and control over protein structure and protein-protein inter-molecular interactions [2]. In addition, other disadvantages include rapid degradation *in vivo* and risks of immunogenicity [3], which further highlight the need for hybridization and creation of multicomponent protein-based biomaterials to achieve tunable functionality and specific biological performance.

Nature has evolved fibrin to serve as the main protein to stop bleeding after trauma and to promote regeneration. Indeed, following rupture of blood vessels, platelets interacting with exposed collagen initiate the coagulation cascade, which ends up with the polymerization of soluble fibrinogen into insoluble fibrin clots. These fibrillary-assembled meshes containing blood cells and key endogenous signals are essential for creating a matrix that stops bleeding, regulates cell infiltration, and ultimately promotes wound healing [4]. From a biomaterial perspective, fibrin represents an exceptional protein-based material for wound repair, being bioresorbable, hemostatic, and immunomodulatory. Hence, it is not surprising that fibrin-based materials, such as Evicel®, Tisseel®, Artiss®, and VeraSeal® have been developed as alternatives to metallic staples and polymeric sutures, leading to clinically-approved regenerative products [5].

Despite their widespread use, fibrin-based materials suffer from three major limitations. First, in terms of bioactivity, fibrin strongly relies on interaction partners, such as heparin, to enhance their ability to sequester and release relevant growth factors over time [6]. Indeed, in the absence of affinity binders, fibrin gels are often accompanied by fast and uncontrolled drug release, hindering any attempt of precise dosing and delivery [4]. Second, fibrin is a soft material characterized by a low mechanical strength (<5 kPa), which is difficult to optimize with precision, as the final mechanical properties strongly depend on intertwining factors [7], such as fibrinogen and thrombin concentrations [8], shear forces [9] and buffers used [10]. Finally, fibrin is highly prone to physical contraction and fast degradation over time, making it practically unsuitable for *in vivo* long-term implantation [11]. Poor mechanics, absence of binding motifs and rapid degradation highlight the need to effective modification strategies to enhance fibrin performance.

Cross-linking agents or complexes with polymeric and inorganic compounds are often employed to overcome the limitations of fibrin, but with limited success. Among cross-linkers, Factor XIIIa, naturally involved in the coagulation cascade, is currently used to create stiffer fibrin matrices [12], while genipin has been used broadly to cross-link amine-displaying molecules, including fibrin scaffolds [13,14]. However, genipin allows tunable cross-linking of fibrin gels but requires careful control of concentration and reaction time to avoid cytotoxicity [15]. Similarly, as Factor XIIIa is enzymatic, it offers less control over cross-linking due to its dependence on substrate availability and reaction kinetics [16]. Mechanically, fibrin has been used in composite formulations involving chitosan, silica, acrylates, polyurethanes, and silk. However, despite these efforts, mixtures of fibrin with other components suffer from visible phase separation and heterogeneous gelation, leading to the formation of partially phase-separated continuous networks, with poor control over the final mechanical properties [17]. Considering these limitations, there is a need for hybrid fibrin materials with precise physico-chemical control.

Enhanced fibrin-based composites with precise properties require a fine control over the functionalization and a hierarchical organization of fibrinogen with additive molecules. In this direction, at the supramolecular level, self-assembling peptides such as peptide amphiphiles (PAs) can be used to create hybrid peptide-protein materials. By tuning PA structure, PAs have been shown to co-assemble [18] with different types of macromolecules [19] into nanofibers that combine the functionality of both the macromolecules and the peptides [20]. For example, PAs can co-assemble with hyaluronan [21], collagen [22], resilin [23], and elastin-like recombinamers [24] to create peptide-protein structures such as membranes [21], particles with different shapes [22], tubular structures [25] and hydrogels [26] with precise control over their final morphology and mechanical properties [25]. Similarly, PAs have been exploited with endogenous ions [27], signaling cytokines and biofluids [26,28,29], to selectively bind, concentrate and release growth factors in a controlled fashion. For these reasons, PAs represent an attractive class of materials to co-assemble with fibrin into supramolecularly-defined peptide-fibrin materials.

At the micro- and macro-scale, contactless biofabrication techniques handling low viscosity, liquid precursors represent appealing strategies to create hierarchically-organized hydrogels [30,31]. Among "nozzle--free" contactless bioassembly approaches [31], sound-guided assembly based on Faraday waves stands out for its numerous advantages to transform biomolecules, such as peptides and proteins, into organized functional composite materials. Opposed to the use of Faraday waves-based techniques, magnetic-based assembly, for example, relies on the use of magnetically-responsive components, such as magnetic nanoparticles, and prolonged exposure to high-intensity magnetic fields, which may affect cellular function and viability of highly sensitive cell types, including stem and progenitor cells [32,33]. Furthermore, generating and controlling magnetic fields with precision is often associated with high costs and complex equipment that makes difficult its integration with standard laboratory workflows. Similarly, optical-based assembly techniques, including optical tweezers or light-driven manipulation, usually demand high-intensity focused light sources, with limited by the light penetration depth in opaque or dense 3D biomaterial networks [34]. Other contactless approaches, including microfluidic and ink jetting carry practical challenges, such as complex fluid handling setups, high costs, and high forces involved in maintaining continuous flows, which may induce cellular stress or damage [35].

On the other hand, sound-guided assembly excels in cytocompatibility and scalability, enabling the simultaneous spatial organization of hundreds to thousands of cells, hydrogel building blocks and inorganic particles at a micrometer-scale resolution precision in a '2.5D' membrane-like configurations. By applying mechanical vibrations from a sound source beneath a container of precursor solution, Faraday waves are generated at the liquid–air interface. These waves produce hydrodynamic drag forces that rapidly (within seconds) drive the assembly toward defined positions at the bottom of the liquid [36]. Such an approach has been increasingly employed to engineer complex 3D *in vitro* systems, including cardiac tissue constructs [37], spatially-organized capillary networks [38], reproducible nerve ingrowth models for low back pain [39], tumor microenvironment models [40], and architectures that mimic hepatic lobule organization [41]. Interestingly, recent advances have extended the use of sound-guided assembly beyond cell aggregation, showing promising potential in the biofabrication of nanometer-to centimeter-scale soft robotic systems [42]. Leveraging on the organization of particles within a hydrogel, new opportunities for manufacturing of complex composite/hybrid material can emerge. Indeed, alongside supramolecular assembly operating at the nanoscale, sound-based assembly can act as a micro- and macroscale 'organizer' of material building blocks to create fibrin-based composite materials with controlled structural and mechanical properties.

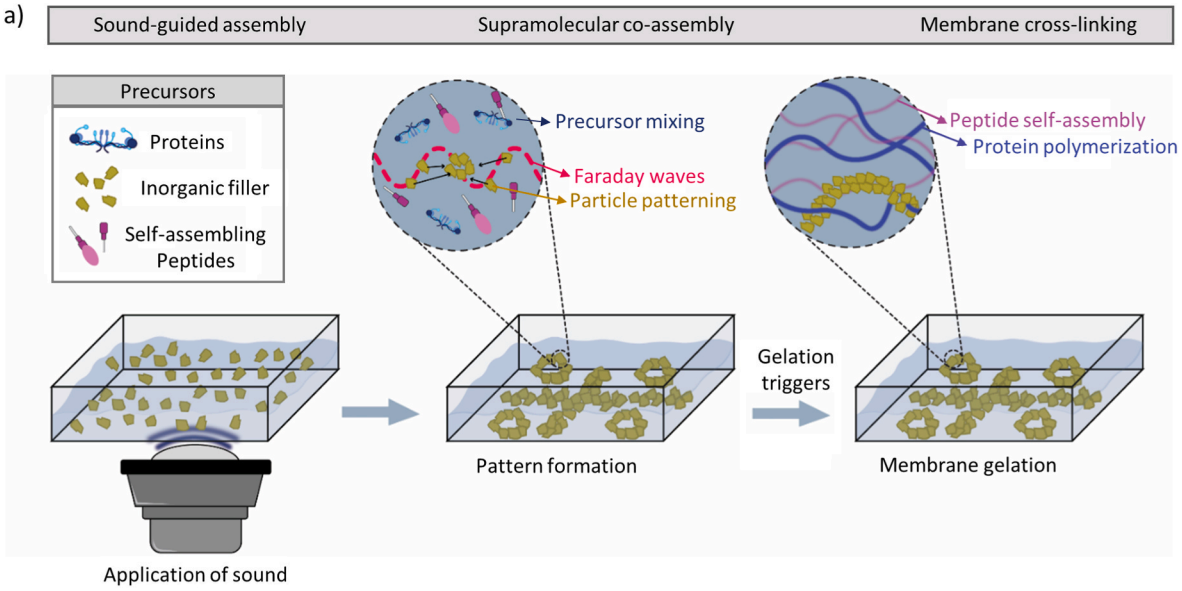
Based on this rationale, in this work we converged supramolecular

and sound-based assembly strategies into a 'one-pot' workflow to create peptide-protein hydrogels with predictable and controlled mechanical and biological properties. As proof-of-concept, we fabricated and characterized a hybrid hydrogel composite membrane based on the co-assembly of PAs with fibrin into a soft matrix containing sound-patterned stiff calcined bone particles (CBPs) (Fig. 1a). Our fabrication process spanned multiple scales of order to achieve functionality. At the nano-to meso-scale, PAs were co-assembled with fibrinogen molecules to create a nanofibrillar mesh able to entrap CBPs into precise patterns. To enrich the fibrin network with precise bioactivity, PAs were designed to show bone morphogenetic protein-2 (BMP-2) binding epitopes (Fig. 1b), enabling precise BMP-2 binding and release over time. At the meso-to macro-scale, stiff and inorganic CBPs were distributed into organized patterns within PA-fibrin gels, enabling the creation of anisotropic CBP-reinforced PA-fibrin composite membranes. For the first time, a theoretical and experimental relationship was demonstrated between the frequency of applied sound waves and the final mechanical properties of the patterned constructs, providing an innovative design-to-function tool for composite hydrogel fabrication. PA-fibrin hydrogels resulted into more stable materials than normal fibrin and were structurally permissive for cell infiltration. Moreover, by exposing our material to peripheral blood mononuclear cells (PBMCs), we demonstrated how immunomodulatory properties of PA-fibrin hydrogels could be modulated by selection of the additive PAs, unlocking new tools for the design of fibrin-based materials with controlled immunomodulatory properties. This study provides a benchmark for biomaterial design, in which supramolecular and acoustic bioassembly are synergistically exploited to create composite materials with rationally-designed shape-to-function features.

2. Results and discussion

2.1. PA-fibrin co-assembly and characterization

A series of *in vitro* preliminary tests were conducted to assess whether fibrinogen was able to co-assemble with PAs to form self-supporting PA-fibrin hydrogels. To understand the effect of peptide charge on the co-assembly, one negatively charged (PA-**E3**) and one positively charged PA sequence (PA-**K3**) were selected for the study (Fig. 2a). With the mindset of creating a clinically-relevant peptide-fibrin composite, a clinically approved version of fibrinogen and thrombin, namely EVICEL®, was selected for the experiments. As shown by zeta potential (Fig. 2b), PA-**K3** was positively charged at neutral pH ($\zeta_{PA\text{-}K3} = 48.77 \pm 1.48$ mV), while PA-**E3** carried a negative charge ($\zeta_{PA\text{-}E3} = -40.1 \pm 1.66$



b)

Molecule	Peptide sequence	MW (kDa)	pI	pH	ζ-potential (mV)	Rationale
PA-**K3**	$C_{15}H_{31}$CONH-VVVAAA-**KKK**-$CONH_2$	1.15	10.3	5	48.8 ± 1.4	Positive charge
PA-**E3**	$C_{15}H_{31}$CONH-VVVAAA-**EEE**-$CONH_2$	1.15	3.4	8	-40.1 ± 1.7	Negative charge and filler
PA-**B3**	$C_{15}H_{31}$CONH-VVVAAA-**EEEGGYPVHPST**-$CONH_2$	1.95	3.8	8	-31.4 ± 2.5	Negative charge and BMP-2-binding epitope

Fig. 1. Fabrication of hydrogel membranes exploiting sound-guided and supramolecular assembly steps. a) The schematic illustrates the multiscale approach converging supramolecular co-assembly and sound-guided hydrodynamic assembly to fabricate peptide-protein hybrid hydrogel membranes. From left to right: A precursor solution containing self-assembling peptides, proteins, and inorganic particle building blocks is exposed to sound-generated Faraday waves that allows a highly controlled spatial arrangement of particles within the precursor volume. The hydrogel solution is then exposed to gelation triggers that synergistically co-assemble peptides and proteins into a fibrillar mesh. b) Table summarizing the key physico-chemical information and rationale of the peptide amphiphile (PA) molecules used in the study. Data are shown as mean ± standard deviation (SD), n = 3 independent samples.

mV). At the same pH, fibrinogen was negatively charged ($\zeta_{Fg} = -6.82 \pm 0.24$ mV), while thrombin showed an overall net positive charge ($\zeta_{Thr} = 7.46 \pm 0.45$ mV). Due to the charge differences between PA-**E3** and PA-**K3**, it is expected that PA-**E3** and fibrinogen molecules will experience a repulsive force in solution, while an electrostatic complexation is expected to occur between PA-**K3** and fibrinogen. As shown in Fig. 2b, a mixture of PA-**K3** with fibrinogen led to a drastic reduction of the peptide's zeta potential ($\zeta_{Fg\ +\ PA\text{-}K3} = 14.53 \pm 1.16$ mV), while an overall negative charge was preserved when fibrinogen was mixed with PA-**E3** ($\zeta_{Fg\ +\ PA\text{-}E3} = -7.13 \pm 0.53$ mV). In both cases, mixtures of PAs and fibrinogen did not produce hydrogels upon contact. Considering the results, it is expected that the final properties of PA-fibrin gels will depend on the charge of selected PAs, as complexation with fibrinogen by PAs could affect the interaction of thrombin with accessible fibrinogen.

To test the effect of PAs on the formation of PA-fibrin hybrid gels, a droplet of activated thrombin solution containing $CaCl_2$ was injected into a droplet of fibrinogen pre-mixed with PA-**K3** or PA-**E3**, as shown in Fig. 2c. In this setup, thrombin will initiate the polymerization of fibrinogen into fibrin, while $CaCl_2$ will trigger the growth of PA cylindrical micelles into elongated nanofibres. As shown in Fig. 2d, injection of thrombin and $CaCl_2$ in fibrinogen plus PA-**E3** produced an immediate gelation of the solution (<5 s), with the formation of a self-supporting hydrogel able to be collected upon retrieval of the pipette tip (Fig. 2d,

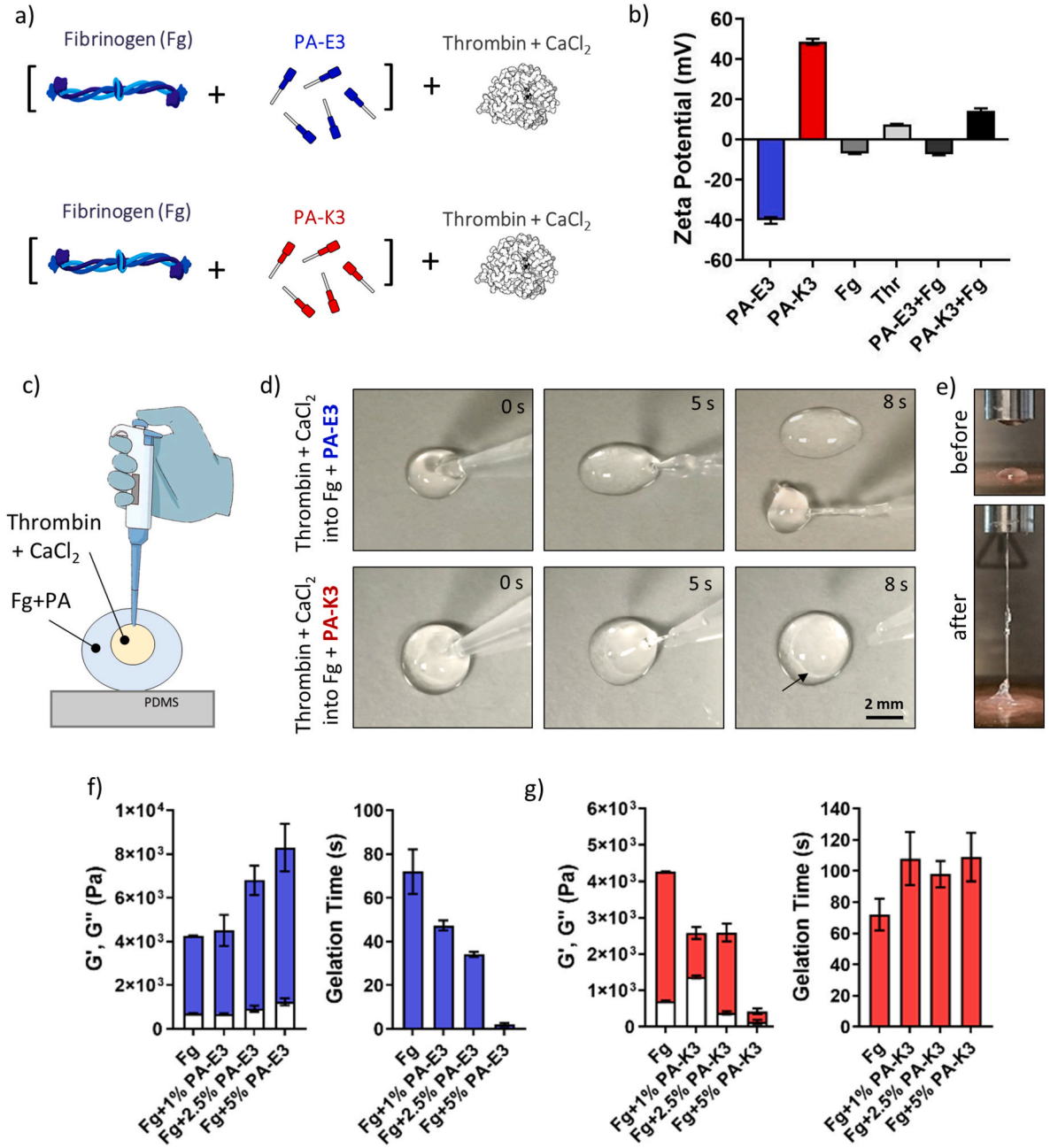


Fig. 2. PA-fibrin co-assembly and characterization. a) Schematics of mixture: fibrinogen is pre-mixed with PAs and then mixed with thrombin solution. b) Zeta potential of PAs, fibrinogen, thrombin and mixtures. c) Schematic diagram of PA-fibrin co-assembly. d) Visual assessment of gel formation after injection of thrombin and $CaCl_2$ into a droplet of PAs pre-mixed with fibrinogen. e) Rheology set-up and visualization of gel formation. f-i) Gel stiffness and gelation time of fibrinogen mixed with (f–g) PA-**E3** and (h–i) PA-**K3** after addition of thrombin and $CaCl_2$. Red and blue bars indicate storage moduli (G′), while white bars indicate loss moduli (G″). Data shown as mean ± standard deviation (SD) and compared using unpaired *t*-test (n = 3 independent; $^{ns}p > 0.05$, $^{*}p < 0.05$, $^{**}p < 0.005$, $^{***}p < 0.001$). (For interpretation of the references to colour in this figure legend, the reader is referred to the Web version of this article.)

first row, 8 s). Conversely, a weak gel was generated after mixing thrombin and $CaCl_2$ with fibrinogen and PA-**K3** (Fig. 2d, second row, 8s). Gelation of PA-**E3**–fibrin was also reproducible in a rheometer-based setup, where a droplet of PA–fibrinogen and thrombin with $CaCl_2$ was pipetted onto the rheometer head and lower plate, respectively, and allowed to react within the set gap, forming an elastic gel once the upper head was raised (Fig. 2e). Exploiting this setup, a series of oscillatory rheology tests were performed to induce *in situ* PA-fibrin gelation and assess the stiffness and the rate of gelation of the formed hydrogels. Both PA-**E3** and PA-**K3** produced self-supporting hydrogels ($G' > G''$) when mixed with fibrinogen and after addition of thrombin and $CaCl_2$ (Fig. S1). Hydrogels reported yield strain values of ~3–4 % across PA sequences, with PA charge and concentration having a remarkable effect on the final mechanical properties of the PA-fibrin gels (Fig. S1). As shown in Fig. 2f, increasing concentrations of PA-**E3** caused an increase in the stiffness of PA-fibrin gels, whose gelation time was drastically reduced from 72 ± 10.2 s to 2.05 ± 0.74 s upon addition of increasing amounts of PA-**E3** (Fig. 2g). The interaction between PA-**E3** and fibrinogen was further investigated by TEM analysis, before addition of thrombin and $CaCl_2$. TEM analysis shows that PA-**E3** alone formed short and homogeneously dispersed single nanofibres of about 10 nm diameter, while fibrinogen aggregated into visible large patches of ~500 nm in width. A 1:1 mixture of PA-**E3** and fibrinogen revealed regions with branched or interconnected PA nanofibres that aggregated into extended three-dimensional microfiber networks. It is expected that, after addition of thrombin and $CaCl_2$, these complexes would take part in the hydrogel formation of PA-fibrin gels, acting as 'nucleation points' for aggregation and providing a structural basis for the accelerated gelation of PA-**E3**-fibrin gels as the PA-**E3** concentration was increased (Fig. S2). To better characterize the nature of these PA-**E3**-fibrinogen interactions, we conducted circular dichroism (CD) spectroscopy analyses. As expected, PA-**E3** exhibited a characteristic β-sheet signal [25], whereas fibrinogen displayed an α-helix conformations, as previously reported [43] (Fig. S3). In contrast, upon mixing, PA-**E3**-fibrinogen displayed a composite spectrum (Fig. S3). The PA-**E3**/fibrinogen (1:1) mixture showed a negative band with increased intensity and a blueshift from 221 to 219 nm, alongside a blueshift of the positive peak from 202 to 198 nm, indicating tighter molecular packing and conformational changes for the PA secondary structure. Additionally, the characteristic α-helix spectrum of fibrinogen was no longer detected, indicating strong PA-fibrinogen interactions and conformational changes for both fibrinogen and PAs (Fig. S3). Moreover, PA-fibrin gels obtained from PA-**E3** were highly stable in PBS over time, with gels being less prone to enzymatic degradation (remaining mass = 95.40 ± 1.39 % after 7 days) by human metalloproteinase-1, known to have fibrinolytic activity [44], compared to pure fibrin (remaining mass = 81.24 ± 1.94 %, Fig. S4).

On the other hand, as also observed by visual inspection in Fig. 2d, addition of PA-**K3** to fibrinogen solutions has a lesser effect on the gelation of PA-**K3**-fibrin. PA-fibrin gels appeared weaker as the content of PAs was increased (Fig. 2h), while overall PA-**K3**-fibrin gels needed more time to undergo gelation compared to native fibrin (109 ± 15.5 s vs 72 ± 10.2 s), independently of the concentration of PA-**K3** supplied (Fig. 2i). The inhibitory effects of PA-**K3** on the gelation kinetics and mechanical stiffness of PA-fibrin hydrogels plausibly arise from the combined action of two distinct physicochemical mechanisms. First, as demonstrated by the electrostatic profiles in Fig. 2b, fibrinogen possesses an overall negative charge at physiological pH, enabling cationic PA-**K3** nanofibres to bind and sequester fibrinogen through electrostatic complexation, thereby reducing its accessibility to thrombin and limiting effective conversion to fibrin. Second, PA-**K3** nanofibres may further inhibit fibrin formation *via* steric hindrance, physically obstructing thrombin's access to its cleavage sites on fibrinogen, and disrupting enzyme–substrate interactions. This dual inhibition mechanism is consistent with observations for other cationic peptides [45], such as D-Phe–Pro–Arg–Pro–Gly (fPRPG) [46], which mimicked fibrinopeptide A and exerted concentration-dependent thrombin inhibition when immobilized on ethylene glycol-terminated self-assembled monolayers (SAMs) through both competitive binding and active site blocking [47]. Coupled together, these results showed that the addition of PA-**E3** to fibrinogen led to PA-fibrin gels with tunable mechanical properties and faster gelation time, as well as higher resistance to enzymatic degradation compared to native fibrin.

2.2. Mechanical and biological functionalization of PA-fibrin gels

Having ascertained that fibrin can be co-assembled with PAs to create tunable PA-fibrin hydrogels, the next step aimed to enrich PA-fibrin with biological and mechanical cues to overcome fibrin's inherent limitations. Fibrin is known to contain inherent bioactive epitopes, including heparin-binding domains, which enable it to directly sequester and retain growth factors over time; however, the incorporation of additional macromolecules, such as heparin, is essential to effectively sequester and retain growth factors over time [6]. In our hybrid fibrin gels design, PAs can play a pivotal role for GF sequestration and release over time, as by designing the chemistry of their hydrophilic head, PAs can self-assemble into nanofibres presenting bioactive function-encoding epitopes on their surfaces. PAs lacking bioactive epitopes, also known as fillers, can be mixed with PAs showing these motifs to create nanofibres with wide ranges of bioactive epitope densities [48,49]. In our study, PA-**E3** sequences acted as filler to be mixed with epitopes binding BMP-2 (PA-**B3** peptide, see sequence in Fig. 1b) to create a class of BMP-2-binding nanofibres (PA-**E3B**). A BMP-2-binding epitope was selected as a proof-of-concept biological functionalization of fibrin, due to the key role played by BMP-2 sequestration and solid-phase presentation for osteogenesis [50]. In our design, the heptapeptide sequence 'YPVHPST' was used as a BMP-2-binding epitope, due to its high affinity reported in phage display with BMP growth factors (GFs) [51]. After assembly, PA-**E3B** nanofibres were capable of physically interacting with and binding free BMP-2 molecules, as suggested by a significant increase in their molecular size upon contact with the growth factor (Fig. 3a). This BMP-sequestering ability was also evident in 3D constructs, when PA-**E3B**-containing hydrogels were able to physically entrap BMP molecules in their network when exposed to BMP-2-containing solutions (Fig. 3b). By tuning the epitope density (*i.e.* ratio of PA-**E3** and PA-**E3** displaying YPVHPST or PA-**B3**) it was possible to tune the amount of BMP-2 that was retained and released over time (Fig. 3c, Fig. S5). PA-**E3B** nanofibres with an epitope density of 5–10 % demonstrated significantly higher BMP-2 binding capacity (19.39 ± 1.74 pg/mL out of 50 pg/mL seeded) compared with control filler PAs lacking a binding epitope (10.31 ± 0.13 pg/mL, $p = 0.0008$). In contrast, nanofibres containing 20–30 % epitope densities showed binding levels that were not significantly different from the 100 % PA-**E3**. When PA-**E3B** self-assembled into hydrogels, bound BMP-2 could be released in a tunable fashion depending on the epitope density of the peptide nanofibres. For instance, a slow and sustained release of BMP-2 was achieved with 1–10 % of PA-**E3B**, when the epitope density was low, while a sigmoidal release was observed for 20–30 % of PA-**E3B**, possibly due to molecular crowding starting to have an effect on the epitope's binding efficiency [49,52,53]. Conversely, a burst release of BMP-2, possibly due to molecule diffusion, followed by sustained profile, was observed for the hydrogel lacking any BMP-binding epitope (filler PA). Finally, by selecting different epitope-displaying PAs, it was possible to bind and release alternative GFs from the BMP family, including TGF-β1 using the heptapeptide 'LPLGNSH' [20,53], making the platform highly modular and versatile (Fig. S6). Considering these results, PAs can be used to modify fibrin and enhance its limitation to bind and release relevant GFs in a controlled fashion.

Alongside bioactivity, fibrin is also known to have poor mechanical properties. Moreover, for bone applications, fibrin alone is known to have poor osteoconductive properties, not able to initiate nor support biomineralization. To overcome these limitations, we explored the

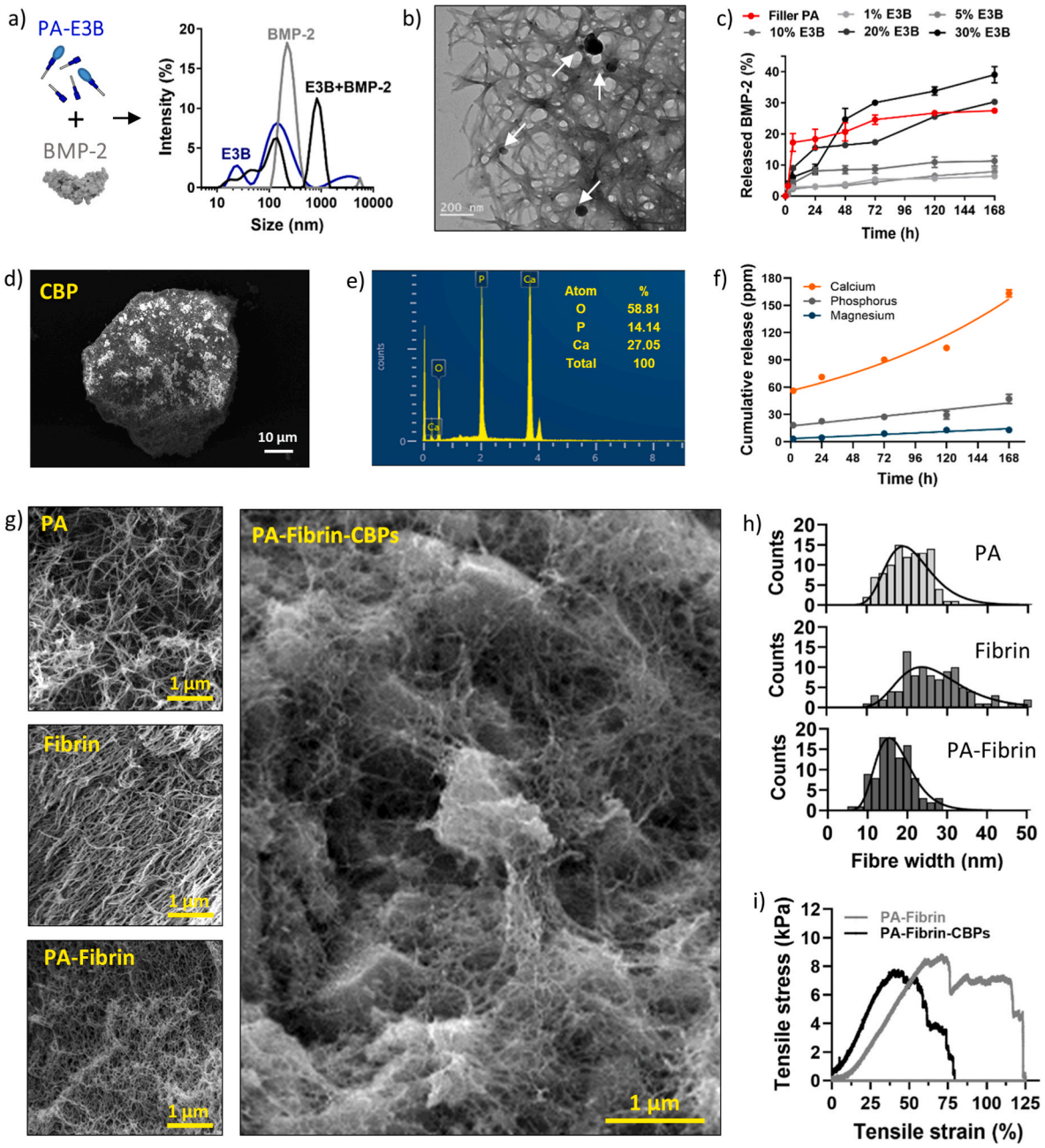


Fig. 3. Biological and mechanical functionalization of PA-fibrin hydrogels. a) Size analysis of PA-**E3B** nanofibres, BMP molecules and PA-**E3B** after exposure to BMP-2. b) BMP-2 molecules (black features indicated by white arrows) entrapped in PA-**E3B** hydrogels. c) ELISA assays of released BMP-2 from PA-**E3B** gels show dependence of release profiles on epitope density. d) SEM image of a CBP. e) EDX analysis of a CBP. f) Cumulative release of calcium, phosphorus and magnesium ions from CBPs dispersed in PBS and measured by ICP-OES. g) SEM images of PA, fibrin, PA-fibrin and PA-fibrin-CBP hydrogel networks with h) their relative fibre diameter distribution. i) Uniaxial load tensile test of PA-fibrin hydrogel membranes with and without addition of CBPs. Data shown as mean ± standard deviation (SD) (n = 3 independent samples).

possibility to incorporate CBPs within PA-fibrin constructs. CBPs are polygonal microparticles obtained from calcination and milling of bones to obtain powders that are highly rich in inorganic mineral components, mainly hydroxyapatite [54,55] (Fig. 3d). Exploiting our experience with the fabrication of CBPs, we produced in house CBPs with a distribution size of 80–180 µm (Fig. S7), within the range of particle size previously used by our group in other sound-driven bio-assemblies [36,38]. For our CBPs, we confirmed the presence of a high content of calcium phosphate products, with a Ca/P ratio of ~1.91, ascribable to mineral structures containing calcium-rich (*e.g.* CaO) or tricalcium phosphates (TCP) phases [56] (Fig. 3e). These phases resulted highly dynamic when dispersed in solution, with release of calcium and phosphorus ions over time, as observed *via* ICP-OES analysis (Fig. 3f). To create reinforced PA-fibrin hydrogel membranes, CBPs were physically dispersed into PA-fibrinogen solutions and then entrapped into PA-fibrin gels upon addition of activated thrombin solution containing $CaCl_2$. The process of PA-fibrin co-assembly did not create a visible phase separation between PA-based and fibrin-based networks, instead the two building blocks synergistically created a hybrid nanofibrillar network with unimodal fibre diameter distribution, as occurs for pure PA and fibrin gels before co-assembly (Fig. 3g). This feature is quite appealing for the generation of fibrin-based materials, as phase separation often represents one of biggest drawbacks for hybrid fibrin-based hybrid materials [4]. Interestingly, the inclusion of PAs induced the formation of a nanofibrillar

hybrid fibrin with thinner fibres ($\mu_{PA\text{-}Fib} = 16.76 \pm 1.32$ nm) compared to normal fibrin ($\mu_{Fib} = 26.1 \pm 1.37$ nm), possibly due to PAs positioning affecting lateral aggregation and width growth of fibrin protofibrils (Fig. 3h). The same fibre diameters were preserved upon addition of CBPs ($\mu_{PA\text{-}Fib\ +\ CBPs} = 17.53 \pm 1.23$ nm). After gelation of the whole composite, CBPs resulted evenly distributed and mechanically interlocked within the PA-fibrin nanofibrillar mesh, as shown in Fig. 3h. In terms of mechanics, the addition of CBPs resulted in a significant

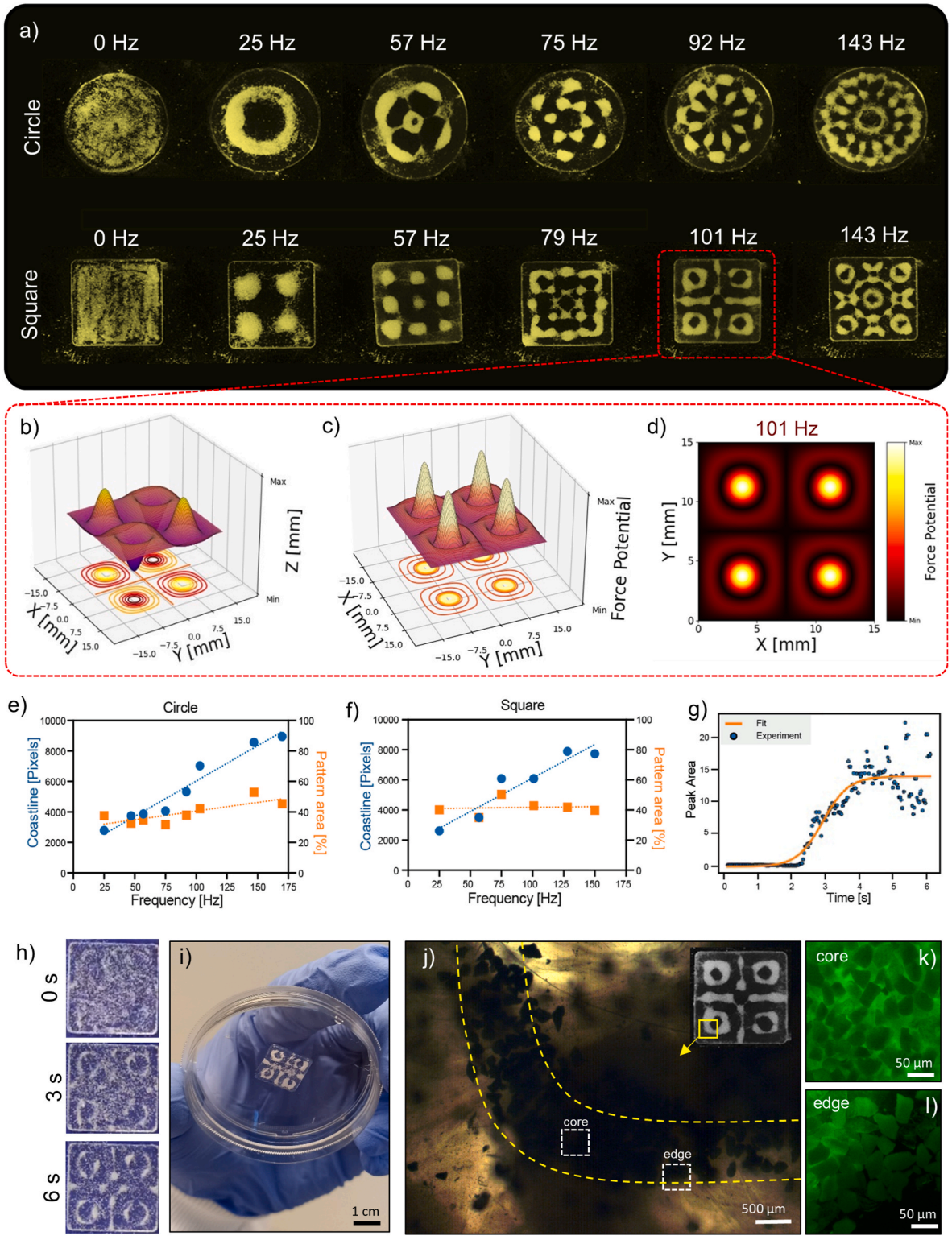


Fig. 4. Sound-guided assembly of functional PA-fibrin-CBP membranes. a) CBP patterns obtained within PA-fibrinogen solutions contained in circle and square containers. b) Surface displacement, c) drag force potential plot and d) its cross-section for a PA-fibrinogen solution excited with sound waves of 101Hz. e) Relationships between pattern coastlines and areas with applied acoustic frequency for e) circle and f) square containers. g) Kinetics of pattern formation. h) Time frames of the CBP pattern formed at 101Hz over time. i) PA-fibrin-CBP hydrogel membrane with pattern induced at 101 Hz. j) Detail of the pattern at 101Hz (quarter of the top left corner ring) under polarised light microscopy. Details on CBP packing at k) core and l) edge of the pattern.

increase of stiffness for PA-fibrin-CBPs ($E = 21.53 \pm 1.90$ kPa) compared with CBP-free counterparts ($E = 18.83 \pm 3.25$ kPa, Fig. 3i). Coupled together, these results showed that fibrin can be 'enhanced' both biologically and mechanically by introduction of bioactive PA sequences and dispersion of inorganic microparticles, creating fibrin-based materials with higher stiffness and enhanced growth factor-binding abilities.

2.3. Fabrication of functional hydrogel membranes via sound-guided assembly

After hydrogel membrane functionalization *via* inclusion of bioactive epitopes and physical entrapment of CBPs, our next step of material engineering exploited sound-guided assembly to create functional hydrogel membranes with dictated microstructures. In our previous works, we harnessed sound-guided Faraday waves and their drag forces to precisely spatially arrange microparticles or cellular aggregates within hydrogel precursors, including gelatin methacryloyl (GelMA), collagen and fibrin, generating reproducible networks and heterogeneous architectures resembling native tissue organization [36,39,40]. This fabrication method features a cost-effective, bench-top wave generator, on top of which a petri dish containing the liquid precursor formulation is securely positioned (Fig. 1a). When activated and tuned with a specific frequency and amplitude, the wave generator allows the formation of Faraday waves onto the precursor surface, thus inducing drag forces within the bulk volume. This physical phenomenon allows objects such as nano- and micro-particles, single cells, or cell aggregates, to be spatially arranged within the hydrogel precursor into specific configurations within seconds. In particular, the formation of patterned structures is highly dependent on the acoustic frequency of the applied sound waves, the geometry of the container as well as the intrinsic properties of the fluid subjected to acoustic waves [38].

Herein, a wide range of frequencies (0–143 Hz) was tested using a container featuring either a circular or a square geometry. By tuning the frequency and the geometry of the container, distinct patterns were generated within the liquid hydrogel precursor, eventually creating different soft nanocomposites in which the fillers (*e.g.*, CBPs) featured a distinct spatial arrangement within their matrices (*e.g.*, PA-fibrinogen solutions). As shown in Fig. 4a, at lower frequency ranges (0–57 Hz), larger and looser patterns were obtained, while higher frequencies (75–143 Hz) led to finer and closer-packed patterns. As observed across the two rows of patterns in Fig. 4a, container geometry further modulated nodal distributions, producing arrangements such as rings (*e.g.* 25Hz), flower-like patterns (*e.g.* 143 Hz) or grid-like lattices (*e.g.* 79, 101 Hz). Numerical simulations of the surface displacements of the hydrogel precursor (Fig. 4b–Video S1) and simulations of the hydrodynamic drag forces generated within (Fig. 4c), highlighted a tendency of the CBPs to cluster in correspondence to areas featuring the lowest force potential, thus characterized by limited turbulence. For instance, at 101 Hz, the areas characterized by the lowest drag forces, corresponded to a pattern featuring four points of symmetry and a central equal-armed cross surrounded by four rings (Fig. 4d). The comparison between the experimental data (Fig. 4a) and the *in silico* simulations (Fig. 4b–d) further strengthened the role of container shape and acoustic frequency as key orchestrators of the sound-driven pattern formation, with a bidirectional relationship between computer simulations and laboratory experiments. The predictability and tunability of the patterns was consistent with previous reports on acoustic-driven assembly, from our lab, although processing other hydrogel precursors [36,39,40]. The viscosity of PA-fibrinogen solutions played a key role in the formation of patterns. In particular, it is worth mentioning that PA-fibrinogen solutions represent an 'ideal' precursor for sound-guided assembly. Indeed, due to the low viscosity, time-dependent and shear-thinning behavior of PA-fibrinogen solutions, these were able to reduce their viscosity upon application of high shear rates, even in cyclic sinusoidal states of sound-simulating shear deformations (Fig. S8). Taken together, these results were essential to understand how acoustic waves interacted with the hydrogel precursor, and with embedded CBPs, to guide the formation of specific CBP patterns within PA-fibrin matrices.

The relationship between acoustic frequency and CBP patterns within PA-fibrin matrices was further analyzed by plotting the patterns' coastlines and areas as a function of the frequency. Fig. 4e–f showed a linear correlation between the increment of the pattern coastlines and the acoustic frequency, while this trend was minimal for the pattern area, regardless of the container shape. We could speculate that an increase in acoustic frequency would lead to smaller wavelengths (nearly punctual for infinite frequencies) that are translated into more densely packed CBP patterns. Conversely, low pitch sound waves with larger wavelengths induce looser patterns of CBPs, as observed for frequencies below 60 Hz. This patterning behavior followed the physics of Faraday wave generation, where higher frequencies lead to shorter wavelengths and more compact structures. Overall, the process of sound-guided bioassembly occurred within tens of seconds, with patterns becoming stable approximately 4 s after the application of acoustic waves (Fig. 4g). Here, experimental data of pattern kinetics followed theoretical expectations, further confirming the reproducibility and predictability of the bioassembly process (Fig. 4g), in agreement with previous kinetics results observed with GelMA matrices [36]. Once CBP patterns were formed within PA-fibrinogen solutions within seconds (Fig. 4h–Video S2), these were then entrapped into PA-fibrin hydrogels by the addition of thrombin and $CaCl_2$ acting as gelation triggers, enabling fibrin polymerization and PA nanofibre growth, respectively. Sound-patterned, PA-fibrin-CBP hydrogel membranes resulted self-supporting upon gelation, withstanding their own weight, as shown in Fig. 4i. The conversion of PA-fibrinogen solutions into ready-to-use hydrogels happened within seconds, retaining CBP patterns with precision. Indeed, contrariwise to other natural polymers, including collagen and gelatin, here gelation of PA-fibrinogen solutions was induced enzymatically (*via* thrombin) and ionically (*via* $CaCl_2$), with no need for temperature switches as triggers of gelation. This feature, achievable with fibrin and with PA molecules, is highly appealing for acoustic-driven material fabrication, as it removes the challenge of dealing with thermo-sensitive precursors, often accompanied with shape distortions after patterning.

The effect of sound waves and Faraday drag forces on the PA-fibrin hydrogel network was also visible at the microscale. Under polarized light, distinct anisotropic patterns within the PA-fibrin matrix were observed after application of sound, with birefringent lines following the curvature of the induced pattern (Fig. 4j). Similarly, alignments of peptide nanofibres under the effect of sound waves have been observed by Ulijn and colleagues, who showed the formation of anisotropic structures at the micrometer scale within tripeptide hydrogel matrices subjected to oscillating pressure waves [57]. On a similar note, Hocking and Dalecki observed micrometric deformation of collagen gels fabricated in the presence of ultrasound [58,59]. With an interest on the arrangement of CBPs, we pre-stained CBPs with calcein and looked at their organization at the microscale after application of sound waves. For instance, in the 'cross-like' pattern at 101 Hz, we observed densely-packed CBPs configurations at the core area of the cross long arm, with CBPs adopting a maximum packing density at the core of the structures (Fig. 4k). Conversely, by moving towards the edges of the patterned arms, it was visible how CBPs were more loosely organized, with a certain level of inter-particle distance that seemed to increase moving away from the core of the patterns (Fig. 4l). This observation provides a visual representation of the effect of the Faraday drag forces on CBPs, which become densely packed at the local minima of the drag force potential (core of the patterns) and loosely arranged moving away from those minima (edges of the patterns). Altogether, these observations highlighted how acoustic frequency can be used to 'sculpt' hydrogel membranes with high level of organization at the microscale.

2.4. Sound-induced patterns-mechanics relationships in hydrogel membranes

Bioconvergence of supramolecular and sound-guided assembly enabled the fabrication of composite hydrogel membranes with high compliance and elasticity. Samples could be stretched multiple times without any delamination of the embedded CBPs from the peptide-fibrin mesh, alongside without any visible loss of the sound-induced pattern (Fig. 5a, Video S3). As the configuration of fillers within a nanocomposite is highly correlated with its bulk mechanical properties, we speculated that for our composite hydrogels, the configuration of CBPs within their PA-**E3B**-fibrin matrix could also affect the final mechanical properties of the composite material. In particular, due to the possibility of using Faraday waves as organizers of CBPs and 'sculptors' of hierarchical structures, we hypothesized that finer patterns obtained at higher sound wave frequencies could exhibit higher mechanical strength compared to coarser ones obtained at lower frequencies. To prove this hypothesis, we ran uniaxial tensile tests on fabricated hydrogel membranes and the stress *vs* strain curves are presented in Fig. 5b. All membranes showed a linear elastic region followed by a plastic behavior, as expected for viscoelastic materials. Analyses of the Young's moduli showed that at 0 Hz, when no sound was applied and when CBPs were randomly organized within the PA-fibrin matrix, hydrogel membranes showed a modulus of $E_{0Hz} = 21.53 \pm 1.90$ kPa, while upon application of 25 Hz and formation of the first pattern, the Young's modulus experienced a drastic drop to $E_{25Hz} = 5.80 \pm 1.01$ kPa (Fig. 5c). This 'softening' effect was expected, as stiffness for composite hydrogels highly depend on the organization of fillers within the matrix and how this propagates internal cracks upon application of a tensile stress. Indeed, increasing frequencies of sound waves induced finer patterns showing shorter distances between CBPs, allowing higher resistance to crack propagation and thus stiffer hydrogel membranes. For instance, patterns created at 101 Hz induced a membrane stiffness of $E_{101Hz} = 14.62 \pm 1.25$ kPa, while at 143Hz we reported a stiffness of $E_{101Hz} = 17.69 \pm 2.36$ kPa. Overall, from the tensile tests, a linear relationship emerged between the frequency applied to form the patterns of CBPs within the PA-fibrin matrix and the bulk stiffness of the PA-fibrin-CBPs composite material.

Intrigued by this behavior, we questioned whether these observations could be generalized and modelled *in silico* to create a toolkit where the stiffness of acoustically-patterned composite hydrogels could be predicted *a priori* starting from the frequency of the sound waves. A similar approach has been applied for the bioplotting of nonapeptide hydrogels, where printing results were modelled starting from the hydrogel viscosities [60]. In this case, finite element method (FEM) simulations were performed to investigate the mechanical response of acoustically-patterned PA-fibrin membranes containing a CBP phase. The primary objective was then to validate whether the patterns generated by acoustic assembly could be used to control and predict the mechanical properties of the resulting composite membranes. In particular, this modeling effort supports the hypothesis that the patterning process enables tunable mechanics based on controlled spatial organization of different the phases (*i.e.* matrix and filler). Starting from the experimental images of the fabricated composite hydrogels, the geometries for the FEM simulations were derived for the frequencies of interest and meshed (Fig. 5d) using linear triangular finite elements for mechanical simulations. Fig. 5e shows the internal strain distributions of the composite hydrogel under tension and how the local deformations across the areas of the hydrogels highly depend on the pattern induced. Stress maps during the loading process up to the maximum value simulated are shown in Videos S4-S6. Low frequencies (*e.g.* 25 and 57 Hz) induced high deformations in the matrix regions bridging CBP agglomerates, while higher frequencies (*e.g.* 101 and 143 Hz) showed a more even distribution of local deformation with lower magnitudes. As observed previously in Fig. 4f, also the FEM analysis showed that experimental pattern area was constant across frequencies and could not explain the stiffness variation (Fig. 5f). Conversely, a linear relationship between the frequency applied to obtain the CBP pattern and the stiffness of the PA-fibrin-CBP hydrogel was observed, which was in line with what observed experimentally (Fig. 5g). Interestingly, by tuning the ratio of Young's moduli of PA-fibrin and CBP phases (E_{ratio}), it was possible to correlate its influence on the global stiffness of the composite (Fig. 5h). Overall, as computed by the FEM analysis, the stiffness of composite hydrogels was still dependent on the frequency of waves applied, with E_{ratio} inversely proportional to the bulk stiffness. This analysis suggested that the mechanical tunability experimentally observed is consistent with physically-plausible variations in the stiffness of the membrane filler. These simulations demonstrated that the mechanical properties of acoustically-patterned PA-fibrin-CBP membranes can be effectively predicted *via* FEM, with geometry and material contrasts extracted directly from experimental data. We envisage that this "frequency-stiffness" relationship could be generalized and applied to the fabrication of alternative sound-assembled composites that are still based on the acoustic patterning of "stiff" particles (*e.g.* organoids, ceramics and glass) or cell aggregates within compatibly softer matrices of precursors (*e.g.* Matrigel, resins and ceramics). This could have wide applicability in sectors such as healthcare (*e.g.* organ-on-a-chip devices and bone plates), engineered living systems (*e.g.* cell aggregates on living matrices) and advanced manufacturing (*e.g.* composite aircraft).

2.5. Influence of hydrogel membrane fabrication on cell positioning and behaviour

For biological applications, we asked ourselves where cells would position themselves within the fabricated membranes once the hydrogels have been patterned and seeded with cells. To do that, after patterning CBPs into a PA-fibrin hydrogel matrix, we seeded MSCs on top on the hydrogel membranes and tracked their position over time. As shown in Fig. 6a, MSCs started to penetrate into the PA-fibrin-CBP hydrogel membranes, reaching the bottom of the gels within 48 h from cell seeding (Fig. 6b). During this timeframe, penetrating MSCs adopted a prominent dual distribution with the CBPs, with cells organising either within or surrounding the patterned CBP particles (Fig. 6c–e). This spatial organisation of MSCs/CBPs resembled the dual distribution of MSCs and microparticles embedded together in liquid precursors and both subjected to sound waves before gelation [38]. In our previous work, for example, we explored the use of both MSC spheroids (Video S7) and β-TCP microparticles as objects to be sound-patterned for the creation of anisotropic hydrogels. When both MSCs and TCPs were exposed to sound waves, a dual distribution of cells and particles emerged, due to the differences in the size and density of the two objects [61]. A dual distribution has also been observed by Pu Chen and colleagues, who assembled induced pluripotent stem cell-derived liver spheroids and endothelial cells into hexagonal cytoarchitectures using acoustic differential bioassembly [41]. The migration of MSCs into the hydrogel membranes, and their arrangement into dual distributions with pre-patterned CBPs, suggests that cell organization is governed by the microarchitectures generated by sound waves within the hydrogel, likely due to localized densification of the network that guides cells into defined configurations. This was further supported by radial colocalization analysis, performed on four independent pattern regions (n = 4) within each hydrogel. Despite slight variability among regions, the profiles showed a consistent trend, with MSCs progressively accumulating in the surroundings or in between the areas of patterned CBPs. MSCs penetrating within the hydrogels remained viable and metabolically active over time, as confirmed by LIVE/DEAD and Presto Blue® assays (Fig. 6f–g). To get further insight on the independent role of the PA-fibrin hydrogel matrix in supporting hMSC infiltration, we performed complementary studies to track hMSC migration within the hydrogel membranes with and without CBPs (Fig. S9). Data show that either PA-fibrin or PA-fibrin-CBP hydrogel

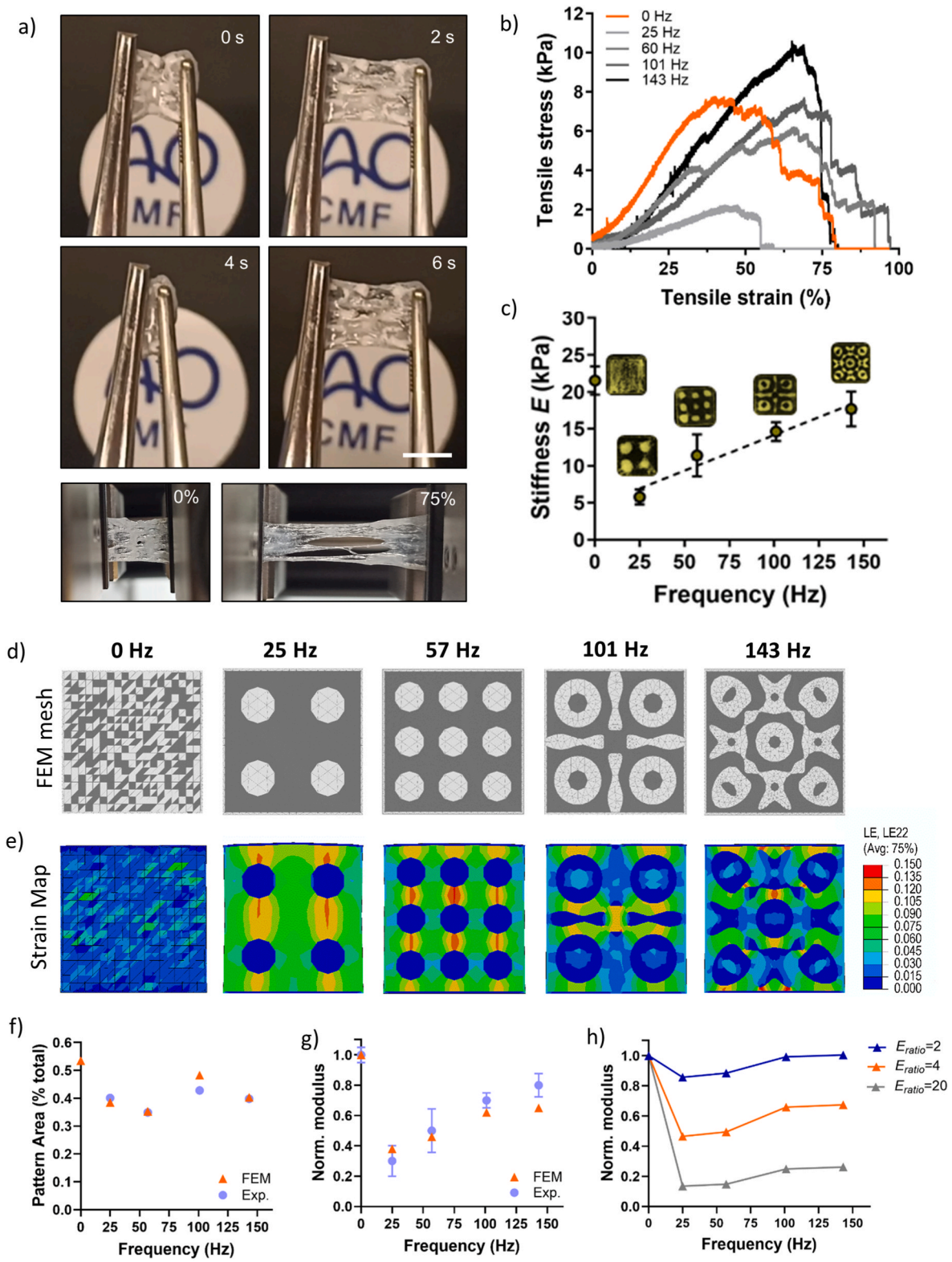


Fig. 5. Experimental and in silico mechanical tests. a) Time-frames of PA-fibrin-CBP membranes stretched multiple times with tweezers (above) and the same membranes at 0 % and 75 % of strain deformations. Scale bar: 5mm b) Tensile tests of PA-fibrin-CBP membranes and c) Young's moduli vs frequency used to induce the sound-based patterns. d) FEM meshes for the five models generated where the subdivision of the two phases is visible (gray = PA-fibrin hydrogel, white = CBPs), and e) logarithmic strain maps in the loading direction at the same maximum loading (linear regime) from FEM simulations of patterned membranes under uniaxial tension. f) Comparison of experimental and FEM measurements of pattern area, expressed as a proportion of the total area of the square membrane. g) Comparison between experimental and simulated Young's moduli (normalized by the 0 Hz modulus). h) Sensitivity analysis showing effective Young's modulus as a function of E_{ratio} for representative patterned geometries. Data shown as mean ± standard deviation (SD) (n = 3 independent samples).

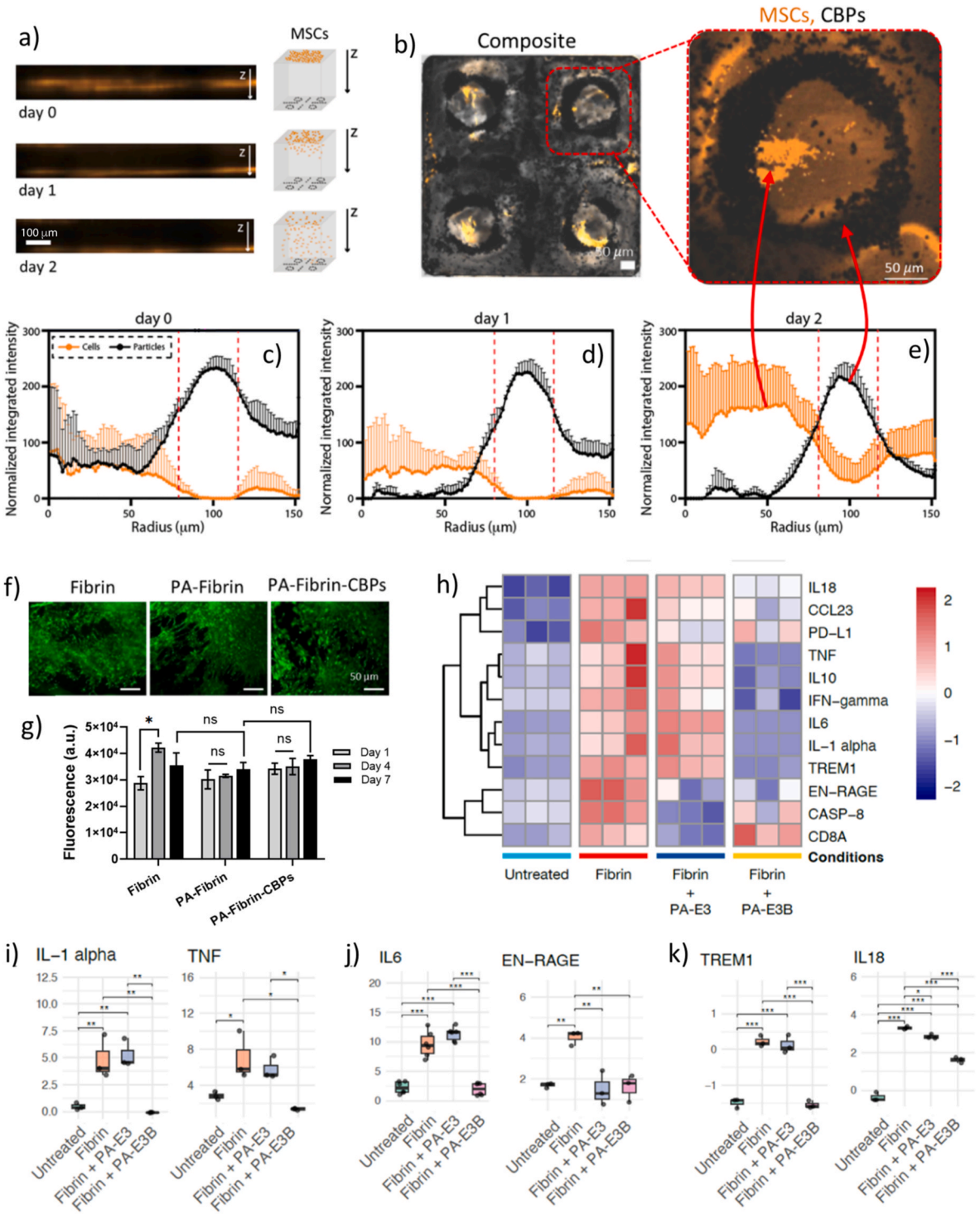


Fig. 6. Sound-based and supramolecular assembly dictate cell organisation and response. (a) Confocal z-stack reconstructions illustrating vertical migration of hMSCs through PA-fibrin hydrogels over time. (b) Overlay of PKH-labelled hMSC membranes (orange) and CBPs (dark spots) confirming co-localization at nodal regions. Data are expressed as mean ± SD across four distinct patterned regions (n = 4 ROIs per time point) within the same hydrogel membrane. (c–e) Radial distribution profiles of hMSCs (black) and CBPs (orange) at day 0, 1, and 2, respectively, showing divergence in migration patterns. (f) Live-cell staining of hMSCs seeded on Fibrin, PA-**E3B**-fibrin, and PA-**E3B**-fibrin-CBPs scaffolds. (g) Quantification of cell proliferation *via* PrestoBlue® metabolic activity assays over 7 days (n = 5). (h) Proteomics heat-map using the Olink Proximity Extension Assay to explore immune and inflammatory responses of PBMCs seeded on culture plastic, fibrin, PA-**E3**-fibrin and PA-**E3B**-fibrin hydrogels. Bar plots of selected markers: i) IL-1α, TNF; j) IL-6, EN-RAGE; k) TREM1 and IL-18. Data shown as mean ± standard deviation (SD) (n = 3 independent samples; $^{ns}p > 0.05$, *p < 0.05, **p < 0.005, ***p < 0.001). Data in Fig. 6g are compared using unpaired *t*-test, data in Fig. 6h–k are compared using Welch's two-sample t-tests. (For interpretation of the references to colour in this figure legend, the reader is referred to the Web version of this article.)

membranes were conducive of cell infiltration, with hMSCs that effectively infiltrated and remained viable within the hydrogel constructs over 48 h, suggesting that the hydrogel substrate itself provides a favourable microenvironment for hMSC migration and survival, independently of the inclusion of CBPs. Interestingly, the presence of CBPs seemed to accelerate hMSC migration, possibly due to sound-induced remodelling of the matrix [62] or attraction towards ions [63,64] released by the CBPs over time, as shown in Fig. 3f. Collectively, these results suggest that microscale patterning can guide cell penetration and organisation acting as microstructural cues that cells leverage for spatial organisation.

As a last step of investigation, we questioned whether tuning the bioactivity of PA-fibrin gels, by choosing different epitope-displaying PAs, could be used to influence cell response. To do this, we composite hydrogels made with PA-**E3B** (binding BMP-2) with PA-**E3** (no bioactivity) and we exposed the materials to peripheral blood mononuclear cells (PBMCs). These cells were selected as they are often used to get an insight into the surface properties of hydrogels and biomaterials once exposed to circulating blood *in vivo* [65,66]. In particular, we were interested to see whether the inclusion of different PAs within PA-fibrin hydrogels could be used as a 'modulator' of PBMC response, due to the interplay between biomaterials design and activation of these immune cells [67]. Towards this goal, targeted proteomic analysis was performed after exposure of PBMCs to the fabricated PA-fibrin gels. Overall, the proteomics analysis revealed distinct alterations in inflammation-related proteins across the experimental conditions. As depicted in the heat-map (Fig. 6h), fibrin alone induced a marked upregulation of several inflammatory markers, including IL-1α, IL-6, TNF, EN-RAGE, TREM1, and IL-18, compared to the untreated group. Notably, exposure of PBMCs to both PA-**E3**-fibrin and PA-**E3B**-fibrin hydrogels substantially attenuated this fibrin-induced inflammatory response. Among the hybrid fibrin hydrogels tested, PA-**E3B**-fibrin gels demonstrated a slightly stronger anti-inflammatory effect, resulting in significant reductions in key early-response pro-inflammatory markers, such as IL-1α, TNF (Fig. 6i), acute-phase response as IL-6, and inflammation modulator markers, such as EN-RAGE, a DAMP molecule often involved as inflammation amplifier *via* RAGE receptor signalling [68] (Fig. 6j). Separate bar plots illustrating IL-18 and TREM1 markers involved as innate immunity coordinators, further confirmed that the introduction of a BMP-2 binding epitope as co-assembly building block within fibrin matrices enabled expression of these markers closer to the baseline levels observed in untreated samples (Fig. 6k), with a better anti-inflammatory effect compared to fibrin co-assembled with PA-**E3** and fibrin alone. Collectively, these findings indicate that PA-**E3** and PA-**E3B** mitigate fibrin-induced inflammation in PBMCs, with PA-**E3B** exhibiting a more pronounced effect. In terms of materials design, these results suggest that through a rational design of hydrogel membrane components, *e.g.* by fine choice of bioactive peptides, it is possible to fabricate sound-pattered peptide-protein hydrogels with dictated cellular responses.

3. Conclusions

In summary, we have demonstrated the possibility to biofabricate composite protein-based hydrogel scaffolds with dictated structure-to-function features by exploiting the bio-convergence of two bottom-up fabrication strategies, namely peptide self-assembly and sound-guided bio-assembly. In particular, we have shown how by starting from fibrin hydrogels it was possible to 'enrich' these materials both mechanically and biochemically by physical entrapment of inorganic microparticles and by chemical incorporation of bioactive functional groups. In detail, by leveraging on the co-assembly of proteins with epitope-displaying PAs, we demonstrated the opportunity to create PA-fibrin hydrogels able to bind and release growth factors, such as BMP-2, for enhanced biological activities, surpassing inherent limitations of traditional fibrin scaffolds. On the other hand, by exploiting the use of sound waves to biofabricate composite scaffolds whose fillers are sound-patterned, we embedded inorganic particles, i.e. CBPs within PA-fibrin hydrogels and we were able to pattern their distribution in final hydrodynamically-organized PA-fibrin-CBPs. By combining experimental testing with *in silico* mechanical simulations, we demonstrated that the frequency of the applied sound waves directly correlates with the stiffness of the resulting composite hydrogels, offering a new strategy to design mechanically robust peptide–protein-based scaffolds Finally, we demonstrated how these new peptide-protein systems can show biological potential *via in vitro* studies and proteomics studies. Based on our results, we believe we have developed a new biofabrication tool in which supramolecular and sound-based assemblies can be used to create multiple peptide-protein materials with dictated structural, mechanical and translational potential. Here, we presented fibrin-based hydrogel composites, but we envisage that a generalization of this concept is possible for other PAs and protein building block combinations. For instance, more complex mixture of proteins and biofluids, such as blood and bone marrow aspirate [28], could be used as protein-rich phases to co-assemble with GF-sequestering PAs, to create 'bio-cooperative' regenerative materials with synergistic properties arising by the means of sound and molecular co-assembly.

4. Experimental section

4.1. Materials

PAs in lyophilized form were purchased from Peptide Synthetics, UK. In particular, two peptides sequences were synthesized, namely PA-**E3** with sequence Palmitoyl-VVVAAAEEE and PA-**B3** with sequence Palmitoyl-VVVAAAEEE-GGYPVHPST. All received peptides were purified by HPLC and purity values > 95 % were used for the study. Human fibrin was purchased as EVICEL® kit (Ethicon, UK) containing one vial of human clottable fibrinogen (55–85 mg/mL) and one vial of human thrombin (800–1200 IU/mL). For this study, fibrinogen was diluted twofold by mixing 1:1 with 1X PBS. Calcined bone particles were produced in-house and kindly supplied by Prof Zhiyu Zhou. If not stated otherwise, all reagents were purchased from Sigma Aldrich, UK.

4.2. PA-fibrin hydrogel formulations

To create PA-fibrin hydrogels, 1 % PA solutions were first created and then mixed with fibrinogen solutions before addition of thrombin. Specifically, for PA-**E3B**-fibrin hydrogels, 0.9 mg of lyophilized PA-**E3** powder was mixed with 0.1 mg of lyophilized PA-**B3** powder and vortexed for 20 s to obtain 1 mg of a powder mixture, namely PA-**E3B**. This mixture was then dissolved in 90 μL of 10 mM HEPES (pH 7.4) and basified with 10 μL of 0.5 M NaOH to create 1 % PA-**E3B** solution. Once the PA-**E3B** solution was made, 17 μL of this was injected into 53 μL of fibrinogen solution and mixed thoroughly to form PA-**E3B**-fibrinogen solutions. Then, 30 μL of thrombin was added to the mixture to induce the gelation and produce 100 μL of PA-**E3B**-fibrin hydrogel. For the PA-**E3**-fibrin and PA-**K3**-fibrin hydrogels, all the steps mentioned above were followed, but 1 mg of either PA-**E3** or PA-**K3** lyophilized powder was used.

4.3. ζ-potential and dynamic light scattering (DLS)

ζ-potential was performed to measure the surface charge of PAs, fibrinogen, thrombin and their mixtures. DLS was used to measure the size of BMP-2 molecules (1 μg/mL) and 1 % PA-**E3B** after incubation. For both techniques, PAs or proteins of interest were diluted into their solvents at a concentration of 0.1 % w/v and solutions were double-filtered with a 0.22 μm syringe-filter before any measurement. ζ-potential and DLS measurements were acquired at 25 °C in triplicate on three independent samples using a Zetasizer Nano-ZS ZEN 3600 (Malvern Panalytical, UK).

4.4. Circular dichroism (CD)

Peptides and proteins secondary structure were assessed by using circular dichroism spectroscopy (CD). Measurements were carried out at 25 °C using a 0.1 cm path length and 300 μL volume quartz cuvette (Chirascan, Applied Photophysics, UK). For secondary structure evaluation, PA-**E3** lyophilized powder was dissolved in MilliQ water and basified with 0.5M NaOH to obtain a final concentration of 0.1 mg/mL. Similarly, human fibrinogen (Sigma Aldrich, code: F3879) was dissolved in MilliQ water at a final concentration of 0.1 mg/mL. To determine PA-protein interactions, PA-**E3** and fibrinogen solutions were mixed on a 1:1 ratio (volume: volume). CD spectra were recorded from 190 to 260 nm with a wavelength step of 0.5 nm. Each spectrum presented in the results is the average of three consecutive readings ($n \geq 3$). The data obtained was normalized to the baseline (MilliQ water as blank control) and the averaged spectrum was smoothed to reduce noise without causing spectrum distortion using the Chirascan software. Between spectra measurements, quartz cuvettes were washed 3x with MilliQ water and purged with nitrogen to minimise minimizes cross-contamination.

4.5. Oscillatory rheology

Oscillatory rheology was performed to track the gelation and check the rheological properties of PA-fibrin gels. All rheological measurements were performed using an Anton Paar MCR102 rheometer (St Albans, UK) using a 8 mm parallel plate geometry and a 0.5 mm gap. To check the gelation time of PA-fibrin gels, 70 μL of PA-fibrinogen solution was placed on the bottom plate of the rheometer and 30 μL of thrombin was positioned on the surface of the 8 mm plate head. The upper head was lowered to allow mixing of thrombin with PA-fibrinogen and a time sweep test was performed immediately. For the time sweep, 0.2 % strain and 1Hz frequency values were used. To check the stiffness of PA-fibrin hydrogels, samples were prepared as described earlier and placed onto the rheometer's static bottom plate while the upper plate was moved to the measuring gap. To measure storage (G') and loss (G'') moduli an amplitude sweep test was performed at 37 °C and 1 Hz in the 0.01–100 % strain range.

4.6. Quantification of BMP-2 binding and release via ELISA

To test the binding ability of PA-**E3B** nanofibres to BMP-2 molecules, PA-**B3** peptides were mixed in lyophilized form with PA-**E3** peptides and vortexed at 200 rpm for 1 min to obtain PA-**B3**: PA-**E3** powder mixtures with mass ratios of 0 %, 1 %, 5 %, 10 %, 20 %, and 30 % w/w. Then, 0.9 mg of PA-**E3**/PA-**B3** powder mixture, namely PA-**E3B**, was dissolved into 90 μL of 10 mM HEPES (pH 7.4) and basified with 10 μL of 0.5 M NaOH to create 1 % PA-**E3B** solutions. PA-**E3B** solutions were then mixed with 1 mM $CaCl_2$ to trigger the formation of PA-E3B cylindrical micelles. At this point, 50 μL of PA-**E3B** solutions were mixed with 50 μL of BMP-2 solutions containing 50 pg/mL of BMP-2 in 1x PBS supplemented with 50 μg/mL BSA. Solutions were then incubated for 1 h at 37 °C, 5 % CO_2 to allow PA-**E3B**-BMP-2 interactions. After incubation, the whole solutions were tested for the presence of unbound BMP-2 using a BMP-2 DuoSet sandwich ELISA assay (code: DY355, R&D Systems, UK). We verified the release ability of PA-**E3B** nanofibers to BMP-2 by studying the release kinetics of the cytokine from a PA-**E3B** hydrogel. In order to form PA-**E3B** hydrogels containing BMP-2, 10 μL of 1 μg/mL of rhBMP-2 were added to 80 μL of 1.25 wt % PA-**E3B** solution and the resulting solution was mixed at room temperature for 30 s at shaking rate of 200 rpm to ensure homogenisation. To trigger gelation of PA-**E3B**, 10 μL of 0.5 M $CaCl_2$ were added to the PA/BMP-2 solution creating 100 μL of 1 wt % PA-**E3B** hydrogels containing BMP-2 molecules. These hydrogels were allowed to equilibrate for 30 min within an incubator (37 °C, 5 % CO_2) before they were exposed to 200 μL of buffer solution (PBS containing 50 μg/mL BSA). At each time point (0, 4, 24, 48, 72, 120 and 168 h) the whole solution in the well was collected and replaced with fresh buffer solution. The amount of BMP-2 in each aliquot was quantified using a BMP-2 DuoSet sandwich ELISA assay (code: DY355, R&D Systems, UK). For this test, six increasing concentrations of BMP-2 binding epitopes were tested by physically mixing PA-**E3** with PA-**B3** powder to get 0 % **E3B** (*i.e.* 100 % PA-**E3** or 'Filler PA'), 1 %, 5 %, 10 %, 20 % and 30 % PA-**E3B**. The cumulative release data points were averaged across three independent replicas and plotted using GraphPad Prism 10 software.

4.7. Transmission electron microscopy (TEM)

TEM was used to assess the nanostructure of the hydrogels in the presence of BMP-2 molecules. Hydrogels were diluted 20-fold with ultrapure water and 20 μL was pipetted on carbon-coated copper TEM grids (EM Resolutions Ltd, UK) for 30 s. Excess solution was carefully removed using Whatman No.1 filter paper and grids were stained with 2 μL of 2 % uranyl acetate for 30 s before washing with 18 μL of ultrapure water. After staining, excess water was removed with filter paper and samples were left to air dry for 1 h. Imaging was performed on a FEI Tecnai Biotwin-12 TEM running at 100 kV and equipped with a Gatan SIS Megaview IV camera.

4.8. Scanning electron microscopy (SEM)

SEM was used to investigate the microstructure of PA-**E3B** and fibrin gels, PA-**E3B**-fibrin and PA-**E3B**-fibrin-CBP composite gels. Moreover, SEM was also used to image CBPs and perform EDX elemental analysis. For the hydrogels, samples were prepared as described above and fixed at room temperature with 4 % paraformaldehyde solution (PFA) for 20 min. Excess of PFA was removed, sample were washed twice with deionised water and dehydrated with a series of increasing ethanol concentrations (20, 30, 50, 70, 90, 96, and 100 %) for 10 min each. Samples were subjected to critical point drying (Leica EM CPD300, Leica, Wetzlar, Germany), mounted on carbon-coated SEM stubs and sputter-coated with iridium (10 nm thick coating) before imaging with an JEOL 7000F FEG-SEM (JEOL Ltd., Tokyo, Japan). A fiber distribution analysis was performed by measuring randomly the lengths of $n = 100$ fibres per sample across three independent SEM images using ImageJ software (v1.54j). For the CBP, particles were directly mounted on carbon-coated SEM stubs and sputter-coated with iridium (10 nm thick). EDX analysis was performed with a JEOL IT-200 (JEOL Ltd., Tokyo, Japan).

4.9. Inductively coupled plasma optical emission spectroscopy (ICP-OES)

To test the stability of CBPs, particles 10 mg of particles were first dispersed into 1 mL of 1X PBS and incubated over time at 37 °C. At each time point (0, 24, 72, 120, 168 h), CBPs were centrifuged at 4000 rpm for 5 min and supernatant was collected for ICP-OES analysis to reveal the amount of ions released. For this test, calcium (Ca), phosphorus (P) and magnesium (Mg) were investigated as ions of interest. ICP-OES was run on a Perkin Elmer Optima 2000 DV ICP-OES with a cyclonic spray chamber, 2.0 mm alumina injector, double monochromator, and a dual backside-illuminated charge-coupled device (DBI-CCD) detector. The instrument was set at 1300W for Ca (RF power) 15 L/min plasma flow rate, 0.2 L/min Auxillary flow rate, 0.8 L/min nebuliser flow rate, radially viewed Ar-ICP. Source equilibration delay of 15 s 2 mL/min sample and wash solution flow rates. Wash time 2 mL/min for 30 s between every sample and standard. For P ions, the instrument was set as above, except axially viewed Ar-ICP and 1400 W (RF power) and 0.4 L/min Nebuliser flow rate. Wavelengths used for Calcium were: 393.4 nm, 396.8 nm, 422.7 nm, wavelengths for phosphorus were 213.6 nm and 214.9 nm, wavelength for magnesium were: (II) 279.6 nm, (II) 280.3 nm, (I) 285.2 nm. Three independent replicates were tested for each wavelength and Scandium was used as internal standard at 1 ppm

monitored at 361 nm. The wash solution, sample and standard solutions were prepared with 2 % nitric acid (prepared with Fisher Scientific S. G. 1.42 70 % Laboratory Reagent Grade).

4.10. Sound-based hydrogel membrane bio-assembly

The sound-based assembly of PA-**E3B**-Fibrin-CBP hydrogel composites started by pipetting 180 μL of PA-**E3B**-fibrinogen solution into the 1 mm-thick containers featuring a square or circular shape, depending on the geometry of the liquid receptacle. CBPs (0.5 mg mL^{-1}) were added to the solution with a spatula and homogenously dispersed across the area of the container. For the sound-controlled assembly system, a polycarbonate frame to contain the CBPs was used. The frame attached to a standard Petri dish using a double-sided adhesive tape. Two geometries were tested: a circular frame (15 mm in diameter) and a square frame (13.4 mm per side). The oscillatory excitation was generated using a PASCO WA-9855 wave driver connected to a function generator. For each driving frequency, the input voltage amplitude (corresponding to the mechanical oscillation amplitude of the driver) was experimentally calibrated, and the resulting amplitude values for all tested frequencies are reported in the Supporting Information (Table S1). The acoustic propagation medium inside the Petri dish chamber is represented by the hydrogel composite precursor with apparent zero shear viscosity of 3.12 ± 0.11 Pas (Fig. S8). Once the wave driver is one, acoustic vibrations are transmitted through the polycarbonate frame, which defines the boundary conditions of the oscillating system. The container material and its dimensions were kept constant in all experiments, ensuring consistent mechanical boundary conditions across different tests. The specific driving frequencies were selected because, at these values, the liquid surface exhibited distinct Faraday-wave resonances, producing well-defined nodal and antinodal regions. These nodal patterns governed the spatial arrangement of the particles, leading to different assembly geometries. Vibrations were applied by tuning the peak-to-peak voltage and frequency until the patterned structures formed within approximately 5 s, as described by Tognato et al. [36] After formation of stable CBP patterns within the PA-**E3B**-fibrinogen solutions, 30 μL of thrombin was added dropwise to induce slow gelation of the PA-**E3B**--fibrin-CBP hydrogel composites, which were left undisturbed at room temperature for 30 min before handling.

4.11. Numerical simulations of the liquid surface displacement by Faraday waves

Numerical simulations of PA-**E3B**-fibrinogen surface displacement driven by hydrodynamic drag forces, were based on the fluid dynamics framework described by Ren et al. and described previously [69]. In brief, this framework reveals that CBPs under sound waves tend to accumulate in regions of minimal potential energy driven by the formation of Faraday waves, which produce standing wave patterns characterized by alternating nodes (areas of minimal displacement) and antinodes (areas of maximal displacement). Displacement at the liquid-air interface were mathematically modelled using Bessel functions of the first kind [70,71]. All simulations were conducted using Python 3.9 with the NumPy and Matplotlib libraries on a personal computer equipped with an 11th Gen Intel(R) i5-1145G7 processor and 16 GB of RAM.

4.12. Mechanical tensile tests

Tensile tests of hydrogels were performed on an Instron 5969 testing machine, loading cell of 100N. Samples (n = 3) were positioned carefully between the clamps and tested at strain rate of 0.5 mm/min at room temperature. The hydrogels' shape was approximated to a parallelepiped with area of 20 × 20 mm^2 and thickness of 4 mm. Young's moduli were extracted from the linear elastic region of force vs displacement curves and reported as average ± standard deviation of three independent samples.

4.13. Finite element modelling (FEM)

The geometries for the FEM simulations were derived from experimental images of membranes patterned under acoustic stimulation at the following frequencies: 25, 57, 101, and 143 Hz. These images were binarized using ImageJ image processing software, and the 2D distribution of the PA phase within the fibrin hydrogel matrix was extracted by identifying relevant points. Constrained spline curves were generated by connecting these points using the Sketcher toolbox in the finite element software ABAQUS. The resulting geometries were then meshed using linear triangular finite elements and used for mechanical simulations. Each model consisted of two material phases: a) A soft matrix phase representing the fibrin hydrogel, and b) A stiffer inclusion phase representing the PA agglomerates. The 0 Hz condition was also simulated by randomly assigning approximately 50 % of the elements the CBP properties and the remaining 50 % the PA-fibrin properties. Due to the irregularity of the mesh, i.e., triangular elements of different areas, this assignment resulted in 53 % of the 2D mesh area being modelled as CBP phase and the remaining 47 % as fibrin phase. These proportions were considered reasonable as it should be noted that the experimental area covered by CBP at 0Hz cannot be accurately assessed due to the random placement of these particles during mixing. All models were square, like the experimental membranes, with an edge of 20 mm. The experimental accumulation of PA particles in the outer perimeter of the membrane was also simulated by adding a 0.3 mm thin frame. In constructing these models, care was taken to reproduce the experimental pattern area, i.e., the surface area fraction of the two phases. The models were subjected to uniaxial tensile loading by applying a uniform tensile force along one edge while constraining the opposite edge. Planar stress conditions were assumed. The FE analysis was static (i.e., no inertia effect) and accounted for geometric nonlinearities during the analysis step. The material properties were linear elastic. The Young's modulus of the CBP phase was assigned to ensure numerical convergence under the simulated tensile load. Since it is experimentally difficult to measure the Young's modulus of each phase, the modulus of the fibrin hydrogel was treated as a tunable parameter by setting the ratio $E_{ratio} = \frac{E_{PA}}{E_{fibrin}}$. A sensitivity analysis was performed over a range of E_{ratio} values to investigate their effect on the effective mechanical response of the patterned membranes.

4.14. Polarized light microscopy

Polarised light microscopy was used to image alignments induced in the composite gels after application of sound waves. Sound-patterned hydrogels were fabricated as described above and imaged with a Zeiss Axioplan microscope equipped with a cross-polarizer.

4.15. Fluorescence light microscopy of CBPs

To image the arrangement of CBPs within sound-assembled hydrogels, 10 mg of CBPs were dispersed into 1 mL of PBS and incubated with 1 μL of Calcein AM (4 μM, Invitrogen L3224) for 2 h at 4 °C under constant agitation. After incubation, CBPs were retrieved from the solution with a Falcon cell strainer of 40 μm mesh size and left to air dry at room temperature overnight. Calcein-stained CBPs were then dispersed into composite hydrogels as described above and imaged with a Leica SP8 upright dipping lens confocal microscope with excitation filter of 495 nm (green, Alexa Flour).

4.16. Human mesenchymal stromal cell (hMSC) culture

Patient-derived hMSCs were previously isolated and expanded from vertebral bone marrow samples (Bern Req-2023-00198) as previously

described. Cells were cultured and further expanded in high-glucose Dulbecco's-modified Eagle medium (Gibco, ThermoFisher, Zürich, Switzerland) with the addition of fetal bovine serum (Corning, Corning, NY, USA) and penicillin, streptomycin (P/S) (Gibco), with a final concentration of 10 % and 1 %, respectively. Once the cells reached 90 % confluence, the medium was removed, and PBS was added to wash out completely the remaining medium. Subsequently, PBS was removed, and 0.05 % Trypsin/EDTA (Gibco) was added. Cells were then incubated at 37 °C for 5 min. After the incubation period, complete medium was added to inactivate Trypsin's action. Detached cells re-suspended in the medium were then centrifuged at 700 rpm for 5 min. Subsequently, the supernatant was discharged, and cells were re-suspended in 1 mL of complete medium to proceed with cell counting. For MSC spheroids, cells were suspended in high-glucose Dulbecco's-modified Eagle medium and cultured on a U-bottom 96-well culture plate.

4.17. hMSC migration and infiltration study

To assess the cell migration and infiltration of hMSCs through the fabricated PA-fibrin-CBP hydrogels, hMSCs were stained with PKH cell membrane staining (code: PKH26GL, Merck, UK) and seeded on the hydrogels with a final concentration of 1×10^5 cells/mL for 48 h. At each time point (4, 24, 48 h), cells were imaged with a Zeiss LSM800 confocal microscope (λ_{ex} 551 nm; λ_{em} 567 nm, PKH26 dye).

4.18. hMSC viability and metabolic activity

Cell viability of MSCs seeded on the composite hydrogels was assessed using a standard LIVE/DEAD staining protocol. After carefully removing the supernatant, cells were rinsed twice with PBS. A staining solution containing Calcein-AM (green; 2×10^{-3} M) and ethidium homodimer-1 (red; 4×10^{-3} M), both from Sigma-Aldrich, was then applied. Samples were incubated in the dark at 37 °C for 30 min. Post-incubation, the staining solution was removed, and samples were washed again with PBS. Fresh complete culture medium was added, and imaging was carried out using an EVOS M7000 fluorescence microscope (ThermoFisher Scientific, Waltham, USA). Metabolic activity of MSCs seeded on composite hydrogels was assessed with PrestoBlue® assay (code: A13261, ThermoFisher Scientific). Composite gels were formed in 96-well plates, MSCs were seeded on hydrogels and incubated with a mixture containing 90 μL of cell culture media plus 10 μL of PrestoBlue® reagent for 10 min at 37 °C and 5 % CO_2. Following incubation, media was collected from the wells and fluorescence was measured using a Tecan Infinite® M-Plex microplate reader (excitaton wavelength: 560 nm; emission wavelength: 590 nm).

4.19. Radial intensity profile and colocalization analysis

To evaluate the radial distribution and colocalization of fluorescence signals within patterned regions, we employed a radial intensity profile approach using the Radial Profile plugin in Fiji (ImageJ). Z-stack images were first projected into a single composite 2D image *via* maximum intensity projection, yielding a representative image for each time point. A circular region of interest (ROI) was then manually drawn around one of the four pattern nodes (circular features), based on visible signal distribution. The same ROI dimensions were subsequently applied to the remaining three pattern nodes within the same sample to ensure consistent sampling across all four regions. Radial intensity profiles were extracted for each ROI, and intensity values were normalized relative to a reference intensity point, typically corresponding to the local maximum or minimum within each pattern. This normalization step allowed comparison of spatial intensity distributions across multiple samples and time points. All results are reported as mean ± standard deviation, calculated from the four ROIs per sample (n = 4 per time point). Data analysis and plotting were performed using GraphPad Prism.

4.20. Peripheral blood mononuclear cell (PBMC) isolation and culture

Peripheral blood mononuclear cells (PBMCs) were isolated using a density gradient centrifugation method. Briefly, blood samples collected in lithium-heparin tubes were diluted with PBS (1:1 for whole blood) and gently layered onto Biocoll at room temperature. After centrifugation at 800*g* for 20 min at room temperature with reduced acceleration and brake settings, the mononuclear cell layer at the interphase was carefully collected. The isolated cells were washed twice with cold PBS containing 2 mM EDTA, followed by centrifugation at 780*g* and 300 g, respectively, at 8 °C. Finally, the PBMC pellet was resuspended in cold complete RPMI medium, passed through a 70 μm cell strainer, and counted using a Neubauer chamber. For culture of PBMCs, 100 μL of PA-**E3**-Fibrin and PA-**E3B**-fibrin hydrogels were prepared into a 96-well plate format, as described in Section 5.2, and the well plate was incubated at 37 °C for 30 min and left undisturbed to permit complete gel formation. Once gel formation was complete, PBMCs suspended in RPMI 1640 medium were added onto the surface of the gels within the 96-well plates and left to adhere.

4.21. Targeted proteomics and bioinformatics analysis

PBMCs were cultured on gels made of fibrin or PA-**E3**-fibrin and PA-**E3B**-fibrin for evaluating targeted proteomic alterations induced by the cell-hydrogel interactions. In details, PBMC cultures, containing 200,000 cells per well in 96-well plates, were exposed to the hydrogels and incubated for 48 h at 37 °C in a CO_2 incubator. Following incubation, samples were collected for targeted proteomics using the Olink Proximity Extension Assay to explore immune and inflammatory responses (Olink Target 96, Inflammation and Immune Response panels, Olink Bioscience, Uppsala, Sweden). Proteomic profiles generated using Olink NPX technology were analyzed using R (v4.4.2). Data import and initial processing were performed using the OlinkAnalyze package (v4.2.0). After removing measurements flagged for low quality and merging the data with experimental metadata, rigorous quality control was conducted. This included assessing data distributions, identifying outliers, and validating the consistency of NPX scaling. To identify differentially expressed proteins, statistical models appropriate for the experimental design were selected; specifically, Welch's two-sample t-tests were applied for comparisons between independent groups. Multiple comparisons were addressed by controlling the false discovery rate (FDR) using the Benjamini–Hochberg procedure, with significance defined as FDR <0.05. Key differential expression results were visualized using volcano plots generated with ggplot2, highlighting effect sizes and statistical significance, and through heatmaps illustrating protein expression patterns across samples.

4.22. Statistical analysis

All experiments were repeated at least three times with at least three replicates ($n \geq 3$). For qualitative results obtained from microscopy techniques (SEM, TEM, fluorescence and polarised light microscopy), at least 3 samples per condition were analyzed and representative images were reported. For quantitative experiments (zeta potential, rheology, ELISA, tensile tests and proteomics analyses) numerical data were reported as mean and standard deviation (SD). Statistical analysis was performed with GraphPad Prism software. A suitable model for statistical analysis was selected depending on the experiments performed and statistical significance was accepted when $p\text{-value} < 0.05$. If not stated otherwise, data were compared with using unpaired *t*-test analysis. For statistical significance, one star (*) denotes p-value <0.05, two stars (**) denote p-value <0.005 and three stars (***) p-value <0.001.

CRediT authorship contribution statement

Cosimo Ligorio: Writing – review & editing, Writing – original draft,

Visualization, Methodology, Investigation, Formal analysis, Data curation. **Alessandro Cianciosi:** Writing – review & editing, Writing – original draft, Methodology, Investigation, Data curation. **Riccardo Tognato:** Writing – review & editing, Software, Methodology, Investigation, Data curation. **Micaela Natta:** Investigation, Data curation. **Romedi Parolini:** Investigation, Data curation. **Sena Ardicli:** Writing – review & editing, Methodology, Investigation, Data curation. **Huseyn Babayev:** Investigation. **Ieva Sapjanskaite:** Investigation. **Samantha L. Kilgour:** Investigation. **Richard Homer:** Investigation. **Bapan Pramanik:** Inverstigation. **Zhiyu Zhou:** Investigation, Funding acquisition. **Andrea Malandrino:** Writing – review & editing, Writing – original draft, Methodology, Investigation. **Eleni Priglinger:** Writing – review & editing. **Cezmi Akdis:** Writing – review & editing, Supervision, Funding acquisition. **Martin J. Stoddart:** Writing – review & editing, Project administration, Funding acquisition. **Alvaro Mata:** Writing – review & editing, Writing – original draft, Supervision, Project administration, Methodology, Investigation, Funding acquisition, Conceptualization. **Tiziano Serra:** Writing – review & editing, Writing – original draft, Supervision, Project administration, Methodology, Investigation, Funding acquisition, Conceptualization.

Conflict of interest

The authors declare no conflict of interest.

Declaration of competing interest

The authors declare that they have no known competing financial interests or personal relationships that could have appeared to influence the work reported in this paper.

Acknowledgements

The work was financially supported by AO Foundation, AO CMF (project: AOCMF-21-04S). AO CMF is a clinical division of the AO Foundation — an independent medically guided not-for-profit organization. AM acknowledges the Medical Research Council (UK Regenerative Medicine Platform Hub Acellular Smart Materials 3D Architecture, MR/R015651/1), the ERC PoC Grant NOVACHIP, and the NIHR Nottingham Biomedical Research Centre at University of Nottingham, Nottingham, UK.

Appendix A. Supplementary data

Supplementary data to this article can be found online at https://doi.org/10.1016/j.mtbio.2025.102643.

Data availability statement

The data that support the findings of this study are available from the corresponding author upon reasonable request.

References

[1] B. Kuhlman, P. Bradley, Nat. Rev. Mol. Cell Biol. 20 (2019) 681.
[2] A. Solomonov, A. Kozell, U. Shimanovich, Angew. Chemie Int. Ed. 63 (2024) e202318365.
[3] D. Yang, J. Xiao, B. Wang, L. Li, X. Kong, J. Liao, Mater. Sci. Eng. C 104 (2019) 109927.
[4] I.V. Roberts, D. Bukhary, C.Y.L. Valdivieso, N. Tirelli, Macromol. Biosci. 20 (2020) 1900283.
[5] W.D. Spotnitz, ISRN Surg. 2014 (2014) 203943.
[6] M.M. Martino, P.S. Briquez, A. Ranga, M.P. Lutolf, J.A. Hubbell, Proc. Natl. Acad. Sci. 110 (2013) 4563. LP.
[7] R.I. Litvinov, J.W. Weisel, Matrix Biol. 60–61 (2017) 110.
[8] J. Wedgwood, A.J. Freemont, N. Tirelli, Macromol. Symp. 334 (2013) 117.
[9] H. Eyisoylu, E.D. Hazekamp, J. Cruts, G.H. Koenderink, M.P.M. de Maat, J. Mater. Sci. Mater. Med. 35 (2024) 8.
[10] N.A. Kurniawan, T.H.S. van Kempen, S. Sonneveld, T.T. Rosalina, B.E. Vos, K. A. Jansen, G.W.M. Peters, F.N. van de Vosse, G.H. Koenderink, Langmuir 33 (2017) 6342.
[11] A. Montero, S. Acosta, R. Hernández, C. Elvira, J.L. Jorcano, D. Velasco, J. Biomed. Mater. Res. 109 (2021) 500.
[12] M. Ehrbar, S.C. Rizzi, R. Hlushchuk, V. Djonov, A.H. Zisch, J.A. Hubbell, F. E. Weber, M.P. Lutolf, Biomaterials 28 (2007) 3856.
[13] C.J. Panebianco, S. Rao, W.W. Hom, J.H. Meyers, T.Y. Lim, D.M. Laudier, A. C. Hecht, M.D. Weir, J.R. Weiser, J.C. Iatridis, Biomaterials 287 (2022) 121641.
[14] M. Likhitpanichkul, Y. Kim, O.M. Torre, E. See, Z. Kazezian, A. Pandit, A.C. Hecht, J.C. Iatridis, Spine J. 15 (2015) 2045.
[15] Z.-S. Xia, E.-W. Hao, Y. Wei, X.-T. Hou, Z. Chen, M. Wei, Z.-C. Du, J.-G. Deng, Comp. Biochem. Physiol., Part C: Toxicol. Pharmacol. 241 (2021) 108951.
[16] L.S. Moreira Teixeira, J. Feijen, C.A. van Blitterswijk, P.J. Dijkstra, M. Karperien, Biomaterials 33 (2012) 1281.
[17] X. Li, W. Rombouts, J. van der Gucht, R. de Vries, J.A. Dijksman, PLoS One 14 (2019) e0211059.
[18] B.O. Okesola, A. Mata, Chem. Soc. Rev. 47 (2018) 3721.
[19] B. Derkus, B.O. Okesola, D.W. Barrett, M. D'Este, T.T. Chowdhury, D. Eglin, A. Mata, Acta Biomater. 109 (2020) 82.
[20] C. Ligorio, A. Mata, Nat. Rev. Bioeng. 1 (2023) 518.
[21] R.M. Capito, H.S. Azevedo, Y.S. Velichko, A. Mata, S.I. Stupp, Science 319 (2008) 1812.
[22] C.L. Hedegaard, E.C. Collin, C. Redondo-Gómez, L.T.H. Nguyen, K.W. Ng, A. A. Castrejón-Pita, J.R. Castrejón-Pita, A. Mata, Adv. Funct. Mater. 28 (2018) 1703716.
[23] B.O. Okesola, H.K. Lau, B. Derkus, D.K. Boccorh, Y. Wu, A.W. Wark, K.L. Kiick, A. Mata, Biomater. Sci. 8 (2020) 846.
[24] A. Majkowska, K.E. Inostroza-Brito, M. Gonzalez, C. Redondo-Gómez, A. Rice, J. C. Rodriguez-Cabello, A.E. Del Rio Hernandez, A. Mata, Biomacromolecules 24 (2023) 4419.
[25] K.E. Inostroza-Brito, E. Collin, O. Siton-Mendelson, K.H. Smith, A. Monge-Marcet, D.S. Ferreira, R.P. Rodríguez, M. Alonso, J.C. Rodríguez-Cabello, R.L. Reis, F. Sagués, L. Botto, R. Bitton, H.S. Azevedo, A. Mata, Nat. Chem. 7 (2015) 897.
[26] Y. Wu, M. Romero, S.N. Robertson, S. Fenn, L. Fisher, I. Willingham, L. Martinez Pomares, C. Ligorio, J. Hill, W. Bu, Z. Zhou, R.D. Wildman, A.M. Ghaemmaghami, H. Sun, J. Sun, M. Cámara, A. Mata, Matter 7 (2024) 216.
[27] C. Ligorio, E. Tavasoli, N. Karaman-Jurukovska, A. Ittycheri, A.M. Kotowska, M. H. Khan, D.J. Scurr, S.A. Gupta, L. V Moogan, J. Emmetsberger, F. Lu, G. K. German, T. Mammone, A. Mata, ACS Appl. Bio Mater. 8 (2025) 2340.
[28] S. Padilla-Lopategui, C. Ligorio, W. Bu, C. Yin, D. Laurenza, C. Redondo, R. Owen, H. Sun, F.R.A.J. Rose, T. Iskratsch, A. Mata, Adv. Mater. (2024) e2407156.
[29] D.W. Barrett, B.O. Okesola, E. Costa, C. Thrasivoulou, D.L. Becker, A. Mata, J. A. Deprest, A.L. David, T.T. Chowdhury, Prenat. Diagn. 41 (2021) 89.
[30] C.F. Guimarães, F. Soto, J. Wang, D. Akin, R.L. Reis, U. Demirci, Curr. Opin. Biotechnol. 77 (2022) 102756.
[31] M. Natta, G. Cocchi, R. Tognato, A. Cianciosi, T. Serra, Adv. NanoBiomed Res. (2025) 2400097 *n/a*.
[32] H. Hu, L. Krishaa, E.L.S. Fong, APL Bioeng. 7 (2023) 31504.
[33] G.F. Goya, L. Asín, M.R. Ibarra, Int. J. Hyperth. 29 (2013) 810.
[34] D. Choudhary, A. Mossa, M. Jadhav, C. Cecconi, Bio-Molecular Applications of Recent Developments in Optical Tweezers, 9, 2019, p. 23.
[35] H.-Q. Xu, J.-C. Liu, Z.-Y. Zhang, C.-X. Xu, Mil. Med. Res. 9 (2022) 70.
[36] R. Tognato, R. Parolini, S. Jahangir, J. Ma, S. Florczak, R.G. Richards, R. Levato, M. Alini, T. Serra, Mater. Today Bio 22 (2023) 100775.
[37] V. Serpooshan, P. Chen, H. Wu, S. Lee, A. Sharma, D.A. Hu, S. Venkatraman, A. V. Ganesan, O.B. Usta, M. Yarmush, F. Yang, J.C. Wu, U. Demirci, S.M. Wu, Biomaterials 131 (2017) 47.
[38] D. Petta, V. Basoli, D. Pellicciotta, R. Tognato, J. Barcik, C. Arrigoni, E. Della Bella, A.R. Armiento, C. Candrian, R.G. Richards, M. Alini, M. Moretti, D. Eglin, T. Serra, Biofabrication 13 (2021) 15004.
[39] J. Ma, J. Eglauf, S. Grad, M. Alini, T. Serra, Adv. Sci. 11 (2024) 2308478.
[40] N. Di Marzio, P. Ananthanarayanan, A.G. Guex, M. Alini, C. Riganti, T. Serra, Mater. Today Bio 16 (2022) 100357.
[41] L. Gu, S. Jiang, X. Xu, J. Wang, F. Xu, H. Fan, J. Shang, K. Liu, U. Demirci, P. Chen, Biofabrication 15 (2023) 15019.
[42] W. Gao, R. Tognato, M. Natta, E. Della Bella, A. Cianciosi, T. Serra, Adv. Intell. Syst. 7 (2025) 2400437.
[43] G. Murano, Semin. Thromb. Hemost. 1 (1974), 01.
[44] K.B. Hotary, I. Yana, F. Sabeh, X.-Y. Li, K. Holmbeck, H. Birkedal-Hansen, E. D. Allen, N. Hiraoka, S.J. Weiss, J. Exp. Med. 195 (2002) 295.
[45] A. Schwienhorst, Cell. Mol. Life Sci. C. 63 (2006) 2773.
[46] J.M. Maraganore, P. Bourdon, J. Jablonski, K.L. Ramachandran, J.W.I.I. Fenton, Biochemistry 29 (1990) 7095.
[47] S.C. Freitas, M.A. Barbosa, M.C.L. Martins, Biomaterials 31 (2010) 3772.
[48] A. Mata, L. Hsu, R. Capito, C. Aparicio, K. Henrikson, S.I. Stupp, Soft Matter 5 (2009) 1228.
[49] H. Storrie, M.O. Guler, S.N. Abu-Amara, T. Volberg, M. Rao, B. Geiger, S.I. Stupp, Biomaterials 28 (2007) 4608.
[50] J. Yang, P. Shi, M. Tu, Y. Wang, M. Liu, F. Fan, M. Du, Food Sci. Hum. Wellness 3 (2014) 127.
[51] S.I. Stupp, J.J.J.M. Donners, G.A. Silva, H.A. Behanna, S.G. Anthony, Self-Assembling Peptide Amphiphiles and Related Methods for Growth Factor Delivery, Google Patents, 2009.
[52] M.J. Webber, J. Tongers, M.-A. Renault, J.G. Roncalli, D.W. Losordo, S.I. Stupp, Acta Biomater. 6 (2010) 3.

[53] R.N. Shah, N.A. Shah, M.M. Del Rosario Lim, C. Hsieh, G. Nuber, S.I. Stupp, Proc. Natl. Acad. Sci. 107 (2010) 3293.
[54] H.Y. Juang, M.H. Hon, Biomaterials 17 (1996) 2059.
[55] J. Ma, W. Guo, M. Gao, B. Huang, Q. Qi, Z. Ling, Y. Chen, H. Hu, H. Zhou, F. Yu, Biofabrication 9 (2017) 45010.
[56] L. Wang, G.H. Nancollas, Chem. Rev. 108 (2008) 4628.
[57] C.G. Pappas, P.W.J.M. Frederix, T. Mutasa, S. Fleming, Y.M. Abul-Haija, S.M. Kelly, A. Gachagan, D. Kalafatovic, J. Trevino, R. V Ulijn, S. Bai, Chem. Commun. 51 (2015) 8465.
[58] E.G. Norris, D. Dalecki, D.C. Hocking, Mater. Today Bio 3 (2019) 100018.
[59] E. Grygotis, D. Dalecki, D.C. Hocking, J. Acoust. Soc. Am. 141 (2017) 4014.
[60] I. Chiesa, C. Ligorio, A.F. Bonatti, A. De Acutis, A.M. Smith, A. Saiani, G. Vozzi, C. De Maria, Modeling the Three-Dimensional Bioprinting Process of β-Sheet Self-Assembling Peptide Hydrogel Scaffolds, 2, 2020, p. 4.
[61] T. Serra, D.O. Eglin, M. Alini, Surface Acoustic Wave (Saw) 3d Printing Method, 2018. United States.
[62] R. Tognato, V. Bonfrate, G. Giancane, T. Serra, Smart Mater. Struct. 31 (2022) 74001.
[63] J.-W. Park, T. Hanawa, J.-H. Chung, Int. J. Nanomedicine 14 (2019) 5697.
[64] T. Qi, J. Weng, F. Yu, W. Zhang, G. Li, H. Qin, Z. Tan, H. Zeng, Biol. Trace Elem. Res. 199 (2021) 559.
[65] H. Amani, M. Alipour, E. Shahriari, J.M. Taboas, Adv. Healthc. Mater. 13 (2024) 2401253.
[66] G. Laverny, A. Casset, A. Purohit, E. Schaeffer, C. Spiegelhalter, F. de Blay, F. Pons, Toxicol. Lett. 217 (2013) 91.
[67] D. Salthouse, K. Novakovic, C.M.U. Hilkens, A.M. Ferreira, Acta Biomater. 155 (2023) 1.
[68] H.J. Kim, M.S. Jeong, S.B. Jang, Int. J. Mol. Sci. 22 (2021).
[69] T. Ren, P. Chen, L. Gu, M.G. Ogut, U. Demirci, Adv. Mater. 32 (2020) 1905713.
[70] J. Lei, Microfluid. Nanofluidics 21 (2017) 50.
[71] N. Di Marzio, R. Tognato, E. Della Bella, V. De Giorgis, M. Manfredi, A. Cochis, M. Alini, T. Serra, Biomater. Biosyst. 14 (2024) 100094.